Chitosan-Derived Nitrogen-Doped Carbon Electrocatalyst for a Sustainable Upgrade of Oxygen Reduction to Hydrogen Peroxide in UV-Assisted Electro-Fenton Water Treatment

Giorgia Daniel,[†,#] Yanyu Zhang,[‡,§,#] Sonia Lanzalaco,[∥] Federico Brombin,[†] Tomasz Kosmala,[†] Gaetano Granozzi,[†] Aimin Wang,[§] Enric Brillas,[‡] Ignasi Sirés**[,‡] and Christian Durante*[,†]

[†] *Department of Chemical Sciences, University of Padua, Via Marzolo 1, 35131 Padova, Italy*

[‡] *Laboratori d'Electroquímica dels Materials i del Medi Ambient, Departament de Química Física, Facultat de Química, Universitat de Barcelona, Martí i Franquès 1-11, 08028 Barcelona, Spain*

[§] *Department of Municipal and Environmental Engineering, Beijing Key Laboratory of Aqueous Typical Pollutants Control and Water Quality Safeguard, Beijing Jiaotong University, Beijing 100044, China*

[∥] *Departament d'Enginyeria Química, EEBE, Universitat Politècnica de Catalunya, C/ Eduard Maristany, 10-14, Ed. I2, 08019, Barcelona, Spain*

Paper submitted to be published in *ACS Sustainable Chemistry & Engineering*

[#] These authors contributed equally to this work.

* Corresponding author: Tel.: +39 0498275112; Fax: +39 0498275829.

E-mail address: christian.durante@unipd.it (C. Durante)

** Corresponding author: Tel.: +34 934039240; Fax: +34 934021231.

E-mail address: i.sires@ub.edu (I. Sirés)

ABSTRACT

The urgency to move from critical raw materials to highly available and renewable feedstock is currently driving the scientific and technical development. Within this context, the abundance of natural resources like chitosan paves the way to synthesize biomass-derived nitrogen-doped carbons. This work describes the synthesis of chitosan-derived N-doped mesoporous carbon in the absence (MC-C) and presence (N-MC-C) of 1,10-phenanthroline, which acted as both porogen agent and as second nitrogen source. The as-prepared MC-C and N-MC-C were thoroughly characterized and further employed as catalytic materials in gas-diffusion electrodes (GDEs), aiming to develop a sustainable alternative to conventional GDEs for H_2O_2 electrogeneration and the photoelectro-Fenton (PEF) treatment of a drug pollutant. N-MC-C presented a higher content of key surface N-functionalities like pyrrole group, as well as an increased graphitization degree and surface area (63 vs. 6 m^2/g), being comparable to commercial carbon black. These properties entailed a superior activity of N-MC-C for the oxygen reduction reaction, as confirmed from its voltammetric behavior at a rotating ring-disk electrode. The GDE prepared with N-MC-C catalyst showed greater H_2O_2 accumulation, attaining values close to those obtained with a commercial GDE. N-MC-C- and MC-C-derived GDEs were employed to treat drug solutions at pH 3.0 by PEF process, which outperformed electro-oxidation (EO). The fastest drug removal was achieved using N-MC-C, needing only 16 min at 30 mA/cm^2 instead of 20 min required with MC-C. The replacement of the dimensionally stable anode by a boron-doped diamond (BDD) accelerated the degradation process, reaching an almost complete mineralization in 360 min. The main degradation products were identified, revealing the formation of six different aromatic intermediates, alongside five aliphatic compounds that comprised three nitrogenated structures. The initial N was preferentially converted into ammonium.

Keywords: Biomass; Electrochemical water treatment; Gas-diffusion electrode; Nitrogen-doped carbon; Organic pollutant; Oxygen reduction reaction

INTRODUCTION

Lately, selected single atoms[1] as well as polyatomic Co-based compounds[2-4] have been successfully tested to electrocatalyze the two-electron oxygen reduction reaction (ORR, reaction (1)) to hydrogen peroxide.

$$O_{2(g)} + 2H^+ + 2e^- \leftrightarrows H_2O_2 \qquad E^0 = 0.695\ V \qquad (1)^5$$

Nonetheless, the development of metal-free electrocatalysts derived from cheap and environmentally friendly biomasses for ORR promotion has become a relevant topic,[6] especially within the context of circular economy. Carbon-based materials combine low cost and environmental impact with high stability, features that make them suitable candidates for H_2O_2 generation in actual devices.[7-9] Likewise, porous carbonaceous materials with N-[10] or S-containing[11] surface functionalities, or both,[12-14] have shown promising electroactivity and selectivity for reaction (1).

To obtain nitrogenated carbon catalysts with high ORR performance and selectivity, three aspects need to be taken into account: (a) the type of N species, which determine the selectivity and the activity of the reaction sites;[10] (b) the architecture, in particular the surface area and porous structure; and (c) the degree of graphitization, which determines the conductivity and stability of the material. Both, experimental studies and theoretical calculations, confirmed that the ORR activity of nitrogen-doped carbon materials originates from the charge delocalization of the carbon atoms due to nitrogen incorporation, which facilitates oxygen adsorption and reduction. The activity was reported to be highly dependent on the doping level and types of nitrogen atoms.[10,12] Nitrogen functional groups can be pinned onto the carbon surface following three different strategies: (i) post-functionalization of undoped carbon, by means of ion implantation,[15] ball milling[16] or grafting;[17] (ii) simultaneous carbonization and doping, feasible via activation procedures like ammonia pyrolysis;[18] and (iii) use of a suitable carbon-nitrogen precursor to carry out the pyrolysis process.[12,13,19-22] Such precursors are N-containing organic molecules or

polymers, such as 1,10-phenthroline and polyaniline, but a plethora of examples starting from biomasses can be found in the literature.[5,23] Examples of transformation of N-containing biomass into N-doped carbons for ORR include the use of cellulose, algae, flowers, fruits or bamboo.[24-32]

Considering any new carbonaceous electrocatalyst of interest, a simple cathode for massive H_2O_2 production could be prepared by coating a three-dimensional substrate, such as a carbon felt.[20,33] This type of substrate enhances the hydrodynamics and mass transport of oxygen,[34] which must be continuously dissolved in the aqueous solution by conventional[33,35,36] or advanced[37] means. Alternatively, the incorporation of an air chamber to the reactor enables a much greater oxygen concentration, thereby enhancing the H_2O_2 production.[5] In such setup, either oxygen or air would be fed to a hydrophobized microporous[38] or macroporous[39] substrate coated with the electrocatalyst, being the ensemble called gas-diffusion electrode (GDE).

Hitherto, GDEs for H_2O_2 electrogeneration have been mostly manufactured using carbon black produced via hydrocarbon pyrolysis,[2,40-44] although other carbon materials like carbon nanotubes[3,4,45] or graphene[46] have also been employed. Fewer insight has been provided on mesoporous carbon,[12,13] whose ordered structure can minimize the residence of the generated H_2O_2 in the reaction zone.[47] Currently, the H_2O_2 production with GDEs finds its main application in water treatment, especially for the degradation of hardly biodegradable organic pollutants through advanced oxidation processes like electro-Fenton (EF) ones.[48-50] In EF, the very reactive $^{\bullet}OH$ generated from Fenton's reaction (2) allows overcoming the limitations of conventional technologies.[51]

$$Fe^{2+} + H_2O_2 \rightarrow Fe^{3+} + {}^{\bullet}OH + OH^- \quad (2)$$

An upgraded version of EF involves the concomitant exposure of the treated solution to UVA light, originating the photoelectro-Fenton (PEF) process,[52] whose main contribution is the photo-induced Fe^{2+} regeneration as follows, favoring its immediate consumption via reaction (2):[3,4,53,54]

$$[Fe(OH)]^{2+} + h\nu \rightarrow Fe^{2+} + {}^{\bullet}OH \quad (3)$$

N-doping of carbons to manufacture GDEs suitable for EF or PEF has been scarcely studied. The presence of N increased the electroactivity of a cathode composed of carbon nanotubes coated with graphene, ending in a faster degradation of dimethyl phthalate by EF.[55] N-doped carbon prepared from 1H-1,2,4-triazole-3,5-diamine showed the highest ORR rate among other materials, yielding a faster EF degradation of sulfathiazole.[56] The number of studies is even lower in the case of biomass-derived carbons for H_2O_2 production with GDEs. As far as we know, Liao et al.[57] have reported the only article on the topic, which discusses the performance of a GDE made of N-doped mesoporous carbon coming from bean dregs. They simply used the cathode to generate H_2O_2 for formaldehyde degradation, which means that the investigation of biomass-derived GDEs in EF and PEF is a quite unexplored field.

Aiming to conceive more eco-friendly EF and PEF approaches for water treatment, herein chitosan has been chosen as a suitable N-containing biopolymeric gel precursor for preparing mesoporous carbon material (MC-C) in virtue of its biocompatibility, biodegradability and high N content (7.1%). It is worth noticing that raw chitosan has been included in some EF systems so far, mainly in the form of composite with iron species to promote heterogeneous Fenton's reaction,[58] although as far as we know it was never incorporated in the form of carbon powder. Chitin and its derivative chitosan are among the most abundant organic compounds in nature, easily obtained from crustacean shells and further purified,[59] which makes them adequate for a wide range of applications.[60] The physicochemical characterization of the synthesized catalysts was performed by different techniques. Their ability to electrogenerate H_2O_2 was assessed by means of cyclic voltammetry (CV) and linear sweep voltammetry (LSV), as well as via bulk electrolyses. In addition, the comparative degradation ability of the two catalysts was investigated by treating 150 mL of acebutolol solutions at acidic pH. The selection of the contaminant is justified by the growing complexity of global water pollution associated to pharmaceuticals due to both, diversity of target molecules and large volume of effluents. Standard water treatments are

frequently unable to ensure total detoxification, which urges more advanced technologies.[61] The hypotensive and antiarrhythmic acebutolol is excreted mostly in its unmetabolized form and hence, it is accumulated alongside its intermediates in surface water,[62] as well as in sewage treatment plant effluents, evidencing a low biodegradability.[63] This represents a serious threat, since acebutolol is toxic for aquatic organisms[64] and causes lupus-like syndrome.[65] Herein, the PEF process was assessed for the first time for acebutolol remediation.

MATERIALS AND METHODS

Chemicals. Chitosan (> 98%, Aldrich for Life Science) and 1,10-phenanthroline (> 99.5%, TCI) were used as received. Other reagents employed for the synthesis of catalysts were: pure ethanol (> 99.8%, Fluka), Nafion® (5 wt % in a mixture of lower aliphatic alcohols and water, Sigma Aldrich), acetic acid (> 99.8%, Sigma Aldrich), acetone (> 99.5%, Sigma Aldrich), H_2SO_4 (95%, Fluka) and NaOH (> 99%, VWR). Each catalyst was mixed with ethanol (96%, Panreac) and polytetrafluoroethylene (PTFE, 60 wt % solution, Sigma-Aldrich), following the procedure described below, to manufacture a GDE. The specific reagents required for the bulk electrolytic trials were: acebutolol (N-[3-acetyl-4-[2-hydroxy-3-(propan-2-ylamino)propoxy]phenyl]butanamide) in the form of a hydrochloride salt ($C_{18}H_{28}N_2O_4$·HCl, CAS number 34381-68-5, Sigma-Aldrich), Na_2SO_4 (anhydrous, Merck) and $FeSO_4·7H_2O$ (Panreac). Acetonitrile and KH_2PO_4 used to quantify acebutolol, as well as CH_2Cl_2 employed in gas chromatography-mass spectrometry (GC/MS), were of high performance liquid chromatography (HPLC) grade from Panreac. Other chemicals needed for the analytical procedures described below included: Ti(IV) oxysulfate (technical grade, Sigma-Aldrich) to determine the H_2O_2 concentration; phenol (99.5%, Sigma-Aldrich), sodium nitroprusside dehydrate (Merck) and ethylenediaminetetraacetic acid disodium salt dehydrate (99%, Alfa Aesar) to quantify ammonium

ion. Ultrapure water for synthesis, manufacture, electrolysis and analysis was obtained from a Millipore Milli-Q system (Merck).

Synthesis of the catalysts. The synthesis of carbon electrocatalysts from chitosan was accomplished by modifying a procedure reported in the literature.[66,67] Chitosan was employed as source of both carbon and nitrogen since it is composed of repeating units of randomly distributed β-(1→4)-linked D-glucosamine and N-acetyl-D-glucosamine. The synthesis consisted in the formation of a chitosan hydrogel followed by the removal of the solvent by freeze drying and the pyrolysis of the resulting material. The hydrogel synthesis involved the dispersion of the chitosan powder (1.8 g) in an acetic acid solution (100 mL, 2 vol %), and the resulting mixture was vigorously stirred to ensure the complete solubilization. In fact, at acidic pH, the amine groups in the N-acetyl-β-(D)-glucosamine moiety are protonated to ammonium (pK_a ($-NH_3^+$) = 6.3),[68] which disrupts the hydrogen bonds between the polymer chains and leads to the collapse of the chitosan crystalline structure and to the solubilization of the polymer in water, finally obtaining a transparent, homogeneous and viscous solution (Figure 1a). The hydrogel formation then occurred by slowly pouring a 1 M NaOH solution to the chitosan viscous solution. Since the diffusion of OH^- ions is slow, the gelation was not instantaneous, but the gelation front advanced at the hydrogel/NaOH solution interphase as the hydroxide ions diffused through the chitosan solution (Figure 1b). The alkaline pH favored the deprotonation of the $-NH_3^+$ groups, promoting the interaction between polymeric chains by hydrogen interactions along with the incorporation of the solution between the chitosan chains, yielding the hydrogel. Once the gelation was concluded, the hydrogel was repetitively rinsed with water until a neutral pH was reached (Figure 1c). Subsequently, the gel was cut into small pieces with a chisel and freeze-dried to remove all water. The dried gel (Figure 1d) was then thermally treated in a two-step pyrolysis procedure.[28] The gel was heated in a Carbolite tubular furnace with a 75 sccm (standard cm^3/min) N_2 flux at 100 °C for 1 h, after which the temperature was raised up to 400 °C at a rate of 5 °C/min and kept at that

temperature for 2 h. The resulting powder (0.72 g) (Figure 1e), was ground by vibro-milling (Retsch MM 400, four steps of 4 min/10–25 Hz) (Figure 1f) and eventually re-pyrolyzed at 900 °C for 2 h under nitrogen atmosphere (Figure 1g). The obtained carbon powder (MC-C, 0.52 g) was washed with water and ethanol, dried at 80 °C overnight and ground by vibro-milling.

Alternatively, phenanthroline was used as secondary source of nitrogen and was added (0.3 g) to the initial chitosan/acetic acid solution, and the mixture was stirred and allowed to gel after the addition of NaOH solution. This procedure allowed to finely disperse phenanthroline all over the hydrogel, avoiding the preferential functionalization of the resulting carbon catalyst and formation of a heterogeneous material. It is worth noting that part of the added phenanthroline was washed away during the neutralization procedure with deionized water, as was confirmed by the presence of the typical UV-Vis adsorption pattern of phenanthroline in the washing water (Figure S1). Conversely, phenanthroline was detected only in traces in the water extracted during the freeze-drying procedure (Figure S1). The resulting dried gel was subjected to a double pyrolysis at 400 and 900 °C, followed by ball milling as in the previous case. The catalyst obtained starting from 1,10-phenthroline and chitosan will be denoted from now on as N-MC-C.

Physicochemical characterization of catalyst powders. Brunauer-Emmett-Teller (BET) analysis, isotherm and pore distribution were performed via nitrogen adsorption-desorption at 77 K using the Micromeritics ASAP2020. The surface area was determined from the desorption curve in a multipoint BET analysis, whereas the pore distribution was analyzed with a slit/cylindric pore NLDFT equilibrium model. Elemental analysis (EA) was carried out using a Thermo Scientific Flash 2000 device. Transmission electron microscopy (TEM) images were obtained by using a FEI Tecnai G2 transmission electron microscope operating at 100 kV. X-ray photoemission spectroscopy (XPS) measurements were performed in an UHV chamber (base pressure $< 5 \times 10^{-10}$ mbar), equipped with a double anode X-ray source (omicron DAR-400), a hemispherical electron analyzer (omicron EIS-125) at room temperature, using non-monochromatized Mg-Kα radiation

192 ($h\nu$ = 1253.6 eV) and a pass energy of 50 and 20 eV for the survey and the single spectral windows,
193 respectively. To perform the XPS measurements, 2.5 mg of carbon powders were dispersed in 1
194 mL of ethanol and then sonicated for 10 min in order to obtain good dispersions; the solutions
195 were then drop-casted onto polycrystalline copper (with a diameter of 6 mm). Raman scattering
196 experiments were conducted with a DXR Raman microscope system (Thermo Fisher Scientific),
197 with a 532 nm laser as the photoexcitation source. The size of the laser spot at the sample was
198 about 25 μm and the power at the sample was 0.1, 0.5 or 1.0 mW.

199 **Electrochemical characterization of catalyst powders.** CV and LSV analysis at a rotating
200 ring disk electrode (RRDE, Metrohm; 5 mm diameter glassy carbon (GC) disk + Pt ring, with a
201 collection efficiency of 25% were performed in both Ar-purged and O_2-saturated 0.0005 M H_2SO_4
202 + 0.050 M Na_2SO_4 solutions by using an Autolab Model 101 N potentiostat/galvanostat. A three-
203 electrode configuration was used, consisting in a GC disk (geometric area of 0.196 cm^2) as working
204 electrode, a graphite rod as counter electrode, and a reversible hydrogen electrode (RHE) as
205 reference electrode. The latter was freshly prepared before each experiment and consisted in a Pt
206 wire mesh sealed to the closed end of a capillary glass tube and refilled with the electrolyte solution
207 from the other open end. H_2 was directly electrogenerated at the Pt wire mesh so that half of the
208 Pt mesh was exposed to the H_2 bubble confined between the electrolyte solution and the closed
209 end of the capillary.[69]

210 The MC-C and N-MC-C catalysts were characterized as thin films prepared by drop-casting
211 an ink (20 μL) of the corresponding carbon powder on a GC disk. Before the drop casting, the GC
212 was polished to a mirror finish with Struers silicon carbide papers of decreasing grain size (grit:
213 500, 1000, 2400, 4000) followed by diamond paste (3-, 1-, 0.25-mm particle size) and repeatedly
214 washed and sonicated (10 min each time) in ethanol for removing all contaminants.

215 All the electrochemical assays were carried out with an optimized loading of 0.6 mg/cm^2. The
216 electrolyte was purged with Ar before each measurement, whereas for the ORR test, high-purity

O_2 gas was bubbled through the electrolyte for at least 1 h to ensure O_2 saturation. The number of electrons transferred during ORR was determined by the RRDE technique. Before data acquisition, the electrocatalysts were first activated by cycling the electrode in the solvent potential window at 200 mV/s until obtaining a stable cyclic voltammogram.

Fabrication of the gas-diffusion cathodes. A GDE was prepared from each type of synthesized powder using the spraying method.[3,4] An appropriate amount (0.1 g) of MC-C or N-MC-C powder was ultrasonically dispersed with PTFE and ethanol for 45 min to obtain an ink (~ 20 mL). Carbon cloth (~8 cm^2 geometric area, BASF B1ASWP), degreased in ethanol and then dried at 60 °C for 3 min, was used as substrate to spray the ink. An air-brush gun fed with N_2 gas was employed to apply several layers, until the ink was finished. After each layer, the material was dried at 60 ºC for 3 min and then weighted. The sample was pressed at 2 ton for 45 s, annealed at 400 °C for 60 min under nitrogen atmosphere and finally cooled down at ambient conditions. The overall weight increment in each GDE was ~80 mg (i.e., MC-PTFE loading of 9.7 mg/cm^2). In order to use any new GDE, it was first activated conducting a galvanostatic polarization in 0.050 M Na_2SO_4 at pH 3.0 for 60 min.

The morphological characteristics of the GDEs before and after use were assessed by scanning electron microscopy (SEM) using a JEOL JSM-7100F field-emission microscope equipped with an energy-dispersive X-ray spectroscopy analyzer. All images were obtained at a voltage of 20.0 kV.

Bulk electrolyses and analyses. Electrolytic trials were conducted for several hours in the absence and presence of pollutant to evaluate the H_2O_2 electrogeneration ability of GDEs and the degradation performance of different processes, respectively. In all these trials, a given GDE (3 cm^2) prepared as described above was placed in a tubular polypropylene housing that received compressed air pumped at 36 L/h, and such cathode was connected to the anode (3 cm^2). The latter consisted in a RuO_2-based plate (i.e., dimensionally stable electrode, DSA) from NMT Electrodes

242 in most of the trials, although boron-doped diamond (BDD) from NeoCoat was also employed in
243 some cases. The distance between the anode and cathode was 1.0 cm. The assays were performed
244 in an undivided glass cell, which was placed onto a magnetic stirrer operated at 700 rpm and
245 contained 150 mL of solution at pH 3.0 and thermostated at 25 ºC. All treatments were made in
246 the presence of 0.050 M Na_2SO_4 as background electrolyte and, when required, acebutolol was
247 added at a concentration of 0.046 mM, i.e., 10 mg/L total organic carbon (TOC). In EF and PEF,
248 Fe^{2+} catalyst was added before starting the electrolysis at a concentration of 0.50 mM. In the photo-
249 assisted treatment, the solution was illuminated with UVA photons from a 6 W Philips tubular
250 lamp (λ_{max} = 360 nm, irradiance of 5 W/m^2) placed above the reactor near the liquid surface.
251 Constant current was always supplied by an Amel 2051 potentiostat-galvanostat, whereas the cell
252 voltage (E_{cell}) was continuously displayed by a Demestres 605 multimeter.

253 When required, the pH of solutions was measured with a Crison GLP 22 pH-meter.
254 Colorimetric analysis of the complex formed between Ti(IV) and H_2O_2 was made using an Unicam
255 UV/Vis spectrophotometer set at λ_{max} = 408 nm, with solutions thermostated at 25 °C. The content
256 of ammonium ion was measured with the same equipment, according to the indophenol blue
257 method, at λ_{max} = 630 nm.[3] TOC was determined using the non-purgeable organic carbon (NPOC)
258 mode of a Shimadzu TOC-VCNS analyzer. Acebutolol concentration was determined by reversed-
259 phase HPLC, with a Waters 600 apparatus equipped with a C18 column at 35 ºC connected to a
260 photodiode array detector. A well-resolved peak appeared at retention time of 4.6 min (λ = 235
261 nm). The mobile phase was a mixture of acetonitrile (40 vol %) and water (10 mM KH_2PO_4 at pH
262 3.0, 60 vol %), circulating at 1.0 mL/min. Trials were made in duplicate and injections in triplicate
263 to correctly assess the drug disappearance. Hence, average values are shown in the figures
264 alongside the error bars (95% confidence level). The final carboxylic acids were quantified as
265 previously reported, by injecting the samples in the same chromatograph but equipped with an

Aminex column.[39] Before each analysis, the samples were conditioned by filtration with PTFE filters (13 mm × 0.45 μm, Whatman).

Current efficiency (CE) values during the H_2O_2 electrogeneration were calculated from the applied charge, according to the Eq. (4):[5]

$$\mathbf{CE}\ (\text{in }\%) = \frac{2F[\mathrm{H_2O_2}]V}{1000M(\mathrm{H_2O_2})Q}100 \qquad (4)$$

where 2 is the stoichiometric number of electrons transferred for ORR to form H_2O_2, F is the Faraday's constant (96,487 C/mol), $[H_2O_2]$ is the concentration of accumulated H_2O_2 (mg/L), V is the volume of the treated solution (L), 1000 is a conversion factor, $M(H_2O_2)$ is the molecular weight of H_2O_2 (34 g/mol), and Q is the charge consumed during the electrolysis.

The mineralization current efficiency (MCE) for each trial at a given electrolysis time t (in h) and applied current I (in A) was calculated as follows:[70]

$$\mathbf{MCE}\ (\text{in }\%) = \frac{nFV(\Delta\mathrm{TOC})_{\mathrm{exp}}}{4.32x10^7 mIt}100 \qquad (5)$$

where n accounts for the number of electrons consumed for the overall mineralization of the drug, $\Delta(TOC)_{exp}$ is the observed TOC decay (in mg/L), 4.32×10^7 is a conversion factor (= 3600 s/h × 12000 mg C / mol) and m is the number of carbon atoms of acebutolol (18 atoms).

The specific energy consumption per unit TOC mass (EC_{TOC}) was obtained as follows:[70]

$$\mathbf{EC_{TOC}}\ (\text{in kWh / g TOC}) = \frac{E_{\mathrm{cell}}It}{V(\Delta\mathrm{TOC})_{\mathrm{exp}}} \qquad (6)$$

where E_{cell} is the average cell voltage (in V).

The primary reaction products were identified by GC/MS. For this, samples collected after selected electrolyses were prepared by liquid-liquid extraction with CH_2Cl_2 as organic solvent.[36] The GC/MS analysis was made in electron impact mode at 70 eV with an Agilent Technologies system: a 6890N gas chromatograph with a 7683B series injector was connected to a 5975 mass spectrometer. Non-polar Teknokroma Sapiens-X5.ms and polar HP-INNOWax columns, both with dimensions of 0.25 μm, 30 m x 0.25 mm (i.d.), were used. When using the former, the

conditions were: temperature ramp starting at 36 ºC for 1 min and increasing up to 320 ºC at 5 ºC/min (hold time 10 min); the temperature of the inlet, source and transfer line was 250, 230 and 300 ºC, respectively, and the analyses were made by splitless (0.7 min) injection, with run time of 67.80 min. When the latter was employed, the conditions were analogous but the final temperature was 250 ºC, with 250 ºC as the temperature of the transfer line and 93.80 min as run time.

RESULTS AND DISCUSSION

Characterization of synthesized catalysts. Nitrogen-doped carbon is a term commonly accepted by the scientific community to classify carbon powder containing nitrogen functional groups. In the present paper, the pyrolysis of the pure dried chitosan hydrogel as well as of the dried hydrogel embedding 1,10-phenanthroline yielded two samples, denoted as MC-C and N-MC-C, respectively. The three-dimensionality of chitosan hydrogels allows the fine dispersion of additives inside the gel structure, which can improve the functionalization of the carbon structure and enhance the textural properties resulting from thermal treatment. A double step pyrolysis, at 400 and 900 °C, was employed for decreasing the burn off of the material, and the resulting black powder was characterized after ball milling.

Figure 2 highlights the TEM images of the two types of carbon powder at different magnifications. The structure of the MC-C sample is characterized by the overlay of compact carbon lamellae (Figure 2a-c), in which any pore structure is clearly visible. The morphological features of MC-C are in part superimposable with those of N-MC-C (Figure 2d-f). However, the lamellar structures are in this latter case characterized by a less packed and compact structure, presenting more jagged edges.

Table 1 reports the elemental analyses of the synthetized carbons. MC-C, prepared by employing the sole chitosan as both carbon and nitrogen precursor, shows a nitrogen fixation of almost 7%, as evidenced by the CHN analysis. Then, it must be clear that the notation MC-C

314 simply means that an additional N-rich precursor was not employed during the synthesis. Also the
315 oxygen content, which in first approximation can be calculated as the residual mass percentage, is
316 sensitively high (~16%). Therefore, it is reasonable to infer that the MC-C carbon was rich in
317 nitrogen and oxygen functional groups, which are extremely important as active sites to
318 electrocatalyze some reactions as well as for increasing the wettability of the electrode material
319 during the electrocatalytic tests. A close comparison with the values obtained for the N-MC-C
320 sample (Table 1) allows noticing that, when 1,10-phenthroline was used as a secondary nitrogen
321 source during the chitosan hydrogel preparation, the resulting carbon had a higher carbon and
322 hydrogen content but a lower nitrogen (< 5%) and oxygen (< 15%) percentage as compared to
323 MC-C. We can presume that the pyrolysis of 1,10-phenanthroline generates small gaseous
324 molecules such as NO, NO_2 and CO, which may act as oxidizing agents able to react with the
325 amorphous part of the carbon structure, i.e., the sp^3 carbon atoms bonded to nitrogen and oxygen
326 functional groups, while the more graphitic sp^2 are preserved, being less prone to react with in situ
327 generated reactive species.

328 The nitrogen adsorption/desorption isotherms at 77 K for MC-C belong to the type II, which
329 is characteristic for non-porous or macroporous materials having a relatively small external surface
330 (Figure 3a). However, the TEM pictures do not show the presence of macropores (Figure 2a-c),
331 which would correspond to pores with diameters wider than 50 nm, being reasonable to conclude
332 that MC-C can be classified as a non-porous carbon material. The sample showed a non-reversible
333 desorption behavior with an open hysteresis loop classified as type-H4, which is often attributed
334 to narrow slit-like pores.[71] The very low value of mesopore volume (Table 1) can be associated to
335 the collapse of the mesopore structure during the gas desorption or to the entrapment of N_2 gas in
336 narrow pores formed between two carbon foil, which could also explain the open hysteresis.[72]
337 However, the experiment was repeated a second time, showing the very same behaviour and hence,
338 the first hypothesis of a carbon structure collapse can be disregarded, being the irreversible

confinement of N_2 molecules between carbon foils the most probable explanation. The extrapolated BET surface area was as small as A_{BET} = 6 m^2/g. Figure 3a also reports the type II nitrogen adsorption/desorption isotherm for N-MC-C. Similarly, in this case the open hysteresis loop can be classified as type-H4, and an analogous conclusion can be drawn regarding the open hysteresis. It is worth noting that the presence of 1,10-phenantroline in the dried hydrogel affected very positively the BET surface area, which was enhanced up to 63 m^2/g in N-MC-C. In this case, the more pronounced uptake at low p/p^o can be associated with an enhanced adsorbent-adsorbate interaction in narrow micropores.[72] The large area was directly related to the increased porosity (Table 1), which was mainly due to micropores (d < 2 nm, V_μ = 0.021 cm^3/g), along with a mesopore fraction (2 nm < d < 50 nm, V_{meso} = 0.017 cm^3/g). The formation of micropores and mesopores or the simple opening of clogged pores can be associated to the reaction of NO, NO_2 and CO gaseous species, generated during the pyrolysis of 1,10-phenanthroline with the carbon structure while CO_2 is released.[73,74] The pronounced uptake at high p/p^o is indicative of the presence of macropores (d > 50 nm), which cannot be in any case evaluated in terms of pore volume and area by the adopted model. However, the presence of a more open and accessible structure finds a confirmation in the TEM images described above. Note that the higher porosity of N-MC-C as compared to MC-C is also evident from the greater total volume (V_{TOT}) summarized in Table 1 (0.065 vs 0.013 cm^3/g, respectively). Therefore, while MC-C is a non-porous carbon material, N-MC-C can be classified as a carbon material with low porosity and textural properties similar to those of commercial carbon black (A_{BET} = 67 m^2/g, V_μ = 0.015 cm^3/g, V_{meso} = 0.137 cm^3/g).

The MC-C and N-MC-C samples were characterized by Raman spectroscopy, which allows elucidating the possible differences in the order and aggregation degree of sites with sp^2 hybridization and, more in general, informs about the amorphous and graphitized degree of a carbon material (Figure 3b).[75] Soft and hard carbon materials typically show two main bands: the

D1 (disorder) at ~1350 cm^{-1} and the G (graphitic) at ~1595 cm^{-1}, as corroborated also for the MC-C and N-MC-C samples. The 2D peak at ~2680 cm^{-1}, ascribed to an out-of-plane vibration mode and generally present in graphite, single layer graphene or highly graphitized carbon is missing, but a broad band between 2400 and 3000 cm^{-1} is present in both samples. The spectra deconvolution revealed the existence of four bands after baseline subtraction and normalization to the maximum of the G band. The two further bands D4 and D3 account for polyenes or ionic impurities and amorphous carbon, respectively. The resulting I_{D1}/I_G band intensity ratio was close to one for both samples (Figure S2). According to the Tuinstra-Koenig model, the following relationship is satisfied:[76]

$$\frac{I(D1)}{I(G)} = \frac{C(\lambda)}{L_a} \quad (7)$$

where $C(\lambda) = -12.6 + (0.033\lambda) \approx 50$ Å, ($\lambda = 532$ nm) and thus, the band intensity ratio can be used to determine the size of the graphite nanocrystallites, which was 4.7 and 5.0 nm for MC-C and N-MC-C, respectively. A close comparison of the two spectra allows observing two main differences: (i) the D1 intensity was higher in the MC-C spectrum than in the N-MC-C one; and (ii) the valley (minimum intensity point) between the D1 and G band was higher in MC-C than in N-MC-C. Both characteristics lead to conclude that N-MC-C was more graphitized than MC-C. This can be further confirmed by considering the D3 band area, responsible for the amorphous carbon, which resulted lower in N-MC-C (37.6 normalized counts) with respect to MC-C (41.6 normalized counts).

The XPS analyses confirmed the presence of nitrogen, oxygen and carbon in both samples (Table 1 and Figure S3). The higher percentage of oxygen in MC-C with respect to N-MN-C confirmed that the introduction of 1,10-phenanthroline contributed to a greater graphitization. Figures 3c and 3d and Table S1 show the C 1*s* XPS data of the analyzed samples. The main carbon component at binding energy (B.E.) = 284.4 eV was attributed to C-sp^2.[12,15,77] At higher B.E. (285.4 eV) the peak corresponded to the sp^3 C-C bond. The higher sp^2/sp^3 ratio in N-MC-C as compared to MC-C sample is in agreement with the observations from Raman analysis (Table S1).

389 There was also a substantial amount of carbon bound to nitrogen or/and to oxygen (peak at 286.4
390 eV). Peaks at B.E. higher than 286.4 eV were due to carbon species bound to oxygen (C=O, O-
391 C=O, O-C(O)-O) or to both oxygen and nitrogen (C-N=O, N-C=O). Peak at 291.1 eV was due to
392 shakeup satellite (π-π^*).

393 The N 1*s* spectra and their deconvolution in single peaks are reported in Figure 3e and 3f. The
394 elemental analysis determined from XPS data indicates a weight percentage of surface nitrogen of
395 2.6% and 3.4% for MC-C and N-MC-C, respectively, in contrast to the above mentioned CHN
396 analysis, which is a bulk sensitive technique that detected a greater nitrogen content in the MC-C
397 sample (Table 1). Therefore, it is reasonable to assert that in the MC-C catalyst the nitrogenated
398 functional groups are mostly confined in the bulk of the carbon material, whereas the pyrolysis of
399 chitosan hydrogel carried out in the presence of 1,10-phenanthroline leads to a higher surface
400 nitrogen content, thereby providing a higher number of available active sites. This is a key finding
401 that justifies the presence of the additional N-containing precursor during the synthesis, since the
402 resulting surface N-functionalities are expected to induce a higher H_2O_2 electrogeneration. The
403 speciation of the singular N 1*s* components evidences the presence of pyridinic, imine, amine and
404 pyrrolic nitrogen (Table 1). Graphitic and nitrogen oxide components were also present in lower
405 percentage.[12,28] It is interesting to observe that the pyrrolic component significantly increases in
406 N-MC-C. Both, pyridinic and pyrrolic nitrogen are beneficial groups since they increase the carbon
407 activity versus ORR and, more in particular, it is reported that pyrrolic nitrogen favors the bi-
408 electronic reduction of oxygen to hydrogen peroxide.[17,27,30]

409 **Electroactivity of chitosan-derived catalysts.** MC-C and N-MC-C were both
410 electrochemically characterized in 0.0005 M H_2SO_4 + 0.050 M Na_2SO_4 as background electrolyte,
411 aiming to determine their activity regarding the oxygen reduction and their corresponding
412 selectivity towards the H_2O_2 generation. Figure 4a and 4b compare the electrochemical behaviour
413 in Ar-purged and O_2-saturated electrolyte using MC-C and N-MC-C electrocatalyst, respectively.

No redox signal appeared in the purged medium, whereas both materials showed electroactivity versus ORR, as deduced from the well-defined reduction peak that was visible in the presence of dissolved O_2. The O_2 reduction peak potential using the N-MC-C (0.525 V vs RHE) was 190 mV more positive than that obtained with the MC-C (0.335 V vs RHE). The smaller overpotential required using the N-MC-C informs about its higher activity with respect to MC-C, which can be attributed to the aforementioned greater content of nitrogen groups on the N-MC-C surface (Table 1).

The ORR may proceed through two pathways: one is a direct four-electron route, which consists in the direct O_2 reduction to water without involvement of H_2O_2 (reaction (8)); the other is a two-step two-electron route in which H_2O_2 is first formed as intermediate via the 2-electron reaction (1), and then it can potentially undergo further reduction via reaction (9).

$$O_{2(g)} + 4H^+ + 4e^- \leftrightarrows 2H_2O \qquad E^0 = 1.229\ V \qquad (8)^5$$

$$H_2O_2 + 2H^+ + 2e^- \leftrightarrows 2H_2O \qquad E^0 = 1.763\ V \qquad (9)^5$$

The selectivity towards the formation of H_2O_2 was evaluated by LSV using an RRDE in O_2-saturated electrolyte at a scan rate of 10 mV/s and rotation speed (ω) of 1600 rpm. During RRDE experiments, the potential of the disk electrode was swept to cathodic values, so that the appearance of a current (I_D) in the linear voltammogram using MC-C and N-MC-C confirmed the reduction of O_2, since this was the sole reducible species present in solution (Figure 4c and 4d, respectively). Due to the electrode rotation, the current increased until a limiting value (I_{lim}) was attained, which depended primarily on the electrode ω, the dissolved O_2 concentration (C_{O_2}), the O_2 diffusion coefficient (D_{O_2}), the solvent kinematic viscosity (ν) and the number of transferred electrons (n), according to the Koutecky–Levich equation:[12]

$$\frac{1}{I} = \frac{1}{I_k} + \frac{1}{I_{lim}} = \frac{1}{nFAkC_{O_2}} + \frac{1}{0.62nFA(D_{O_2})^{2/3}\nu^{-1/6}C_{O_2}\omega^{1/2}} \qquad (10)$$

where I_k is the kinetic current and I_{lim} is the diffusion limiting current. In such setup, the electrode rotation pushes the electrogenerated species toward the ring electrode, which is polarized at a fixed

potential (E_{ring} = 1.50 V vs. RHE), at which H_2O_2 can be easily reoxidized to H_2O. If H_2O_2 is generated at the disk electrode, it can then be detected at the ring electrode and a ring current (I_R) can be recorded in the case of MC-C and N-MC-C (Figure 4c' and 4d', respectively). The number of exchanged electrons can be in principle be determined by plotting the reciprocal of the total instant current (I^{-1}) versus $\omega^{-1/2}$, whenever all the other specific parameters are known. However, this procedure can bring to misleading results when, for example, the catalyst layer is not homogeneous and sufficiently thin. Alternatively, the number of electrons involved in the ORR and the yield of hydrogen peroxide ($y_{H_2O_2}$) can be obtained from the I_D (in A) and I_R (in A) values measured at the RRDE, according to Eqs. (11) and (12):[72]

$$n = \frac{4I_D}{I_D + {I_R}/{N}} \quad (11)$$

$$y_{H_2O_2} = 100\,\frac{2I_R}{NI_D + I_R} \quad (12)$$

where N is the collection efficiency (N = 0.25). The half-wave potential, which can be determined from the RRDE measurements, confirmed the higher catalytic activity of N-MC-C ($E_{1/2}$ = 0.437 V) as compared to MC-C ($E_{1/2}$ = 0.288 V). Furthermore, the n values were 3.55 and 3.76, using N-MC-C and MC-C, respectively, which informs about the superior selectivity versus H_2O_2 generation using the former electrode. In fact, the hydrogen peroxide yields ($y_{H_2O_2}$, Figure 4c'' and 4d'') were 25% (N-MC-C) and 11% (MC-C). At first sight, these values could seem to far from n = 2 and $y_{H_2O_2}$ = 100% ideally expected from an electrocatalyst that fully promotes the two-electron ORR, without further H_2O_2 reduction or simultaneous reaction (5). Nonetheless, the main goal within the context of this work was not the development of an optimum electrocatalyst for H_2O_2 electrosynthesis, but the synthesis of a potentially cheaper and more eco-friendly material to electrogenerate sufficient amounts of H_2O_2 for its direct application in Fenton-based electrochemical water treatments. Therefore, bulk electrolyses were conducted in order to assess the ability of GDEs, prepared with the synthesized MC-C and N-MC-C, to accumulate H_2O_2.

A series of long galvanostatic electrolyses was carried out, at different current densities from 10 to 60 mA/cm^2, to monitor the concentration of H_2O_2 accumulated in a 0.050 M Na_2SO_4 solutions at pH 3.0 for 360 min. In these trials, either an MC-C- or N-MC-C-derived GDE was connected to a DSA plate. As can be seen in Figure 5a, with both types of GDE, a higher concentration was achieved as the electrolysis progressed, as a result of the effective ORR via reaction (1). However, the initially linear trends became curves after 120-180 min, which means that the processes that accounted for the H_2O_2 destruction gradually became more significant. The main ones among them were: (i) the cathodic reduction via reaction (6), (ii) its oxidation at the anode surface, since the cell had one single compartment, and (iii) the chemical decomposition and natural disproportionation in the bulk. In fact, a final plateau could be observed in some cases, especially at the highest current density of 60 mA/cm^2, which was reached once the H_2O_2 formation and destruction rates became equal. At 360 min, the concentrations attained at 10, 30 and 60 mA/cm^2 were 3.68, 9.35 and 9.75 mM using the MC-C, and 5.20 13.2 and 15.3 mM with the N-MC-C. Therefore, the greatest values appeared in the cells with the N-MC-C-derived GDE, regardless of the applied current density, which confirms the importance of the superficial N content and the corresponding N-functionalities described above. Furthermore, the difference was higher as the current density was increased (i.e., the curves with both GDEs were comparatively more separated), suggesting a relatively greater stability of the N-MC-C under more aggressive conditions. In fact, using the MC-C-derived GDE, the H_2O_2 contents at 30 and 60 mA/cm^2 were very close, meaning that the stability range for that cathode was more limited. Such lower stability can be related to its structural characteristics, discussed above, since a lower porosity and greater compactness constitute a barrier that oxygen gas tends to break in a rough manner.

A comparison with reported values for H_2O_2 accumulation in similar setups that employed commercial C-PTFE GDEs allows concluding that the electrogeneration performance observed in this work is in the same range, in particular in the case of the GDE prepared with the N-MC-C.

For example, 0.59 mM H_2O_2 (vs 2.00 mM in this work) were measured at 30 min in a 0.050 M Na_2SO_4 solution at pH 3.0 recirculated at a liquid flow rate of 4.4 L/min and electrolyzed at 30 mA/cm^2 in a pilot plant, whereas a content of 17 mM H_2O_2 was achieved after 360 min at 50 mA/cm^2 in a 2.5 L plant.[78] Moreover, the values represented in Figure 5a are much better than those typically attained with raw carbon-felt cathodes, which have also been employed in EF and PEF treatments.[5] These results corroborate that the electroactivity of the synthesized catalysts was high enough to accumulate H_2O_2, despite the partial selectivity discussed from Figure 4. For a more accurate comparison with the literature, Table S2 summarizes the current efficiency, H_2O_2 mass production rate and H_2O_2 yield calculated for our best catalyst as well as for carbon electrocatalysts employed in GDEs for water treatment. Note that, despite the moderate efficiency of the new material to accumulate H_2O_2, the crucial finding of this work is that the electrogenerated amount is sufficient to promote the degradation of water pollutants (see subsections below).

The presence of Fe^{2+} in the solution (i.e., EF conditions) should cause a drastic reduction in the quantity of H_2O_2 accumulated due to its quick decomposition via Fenton's reaction (2). Indeed, this is verified in Figure 5b, which shows similar profiles regardless of the type of cathode when Fe^{2+} at a concentration of 0.50 mM was employed as catalyst. The other conditions were analogous to those described in Figure 5a, at 30 mA/cm^2. Based on the almost identical trends to finally attain a value of ~5.1 mM H_2O_2, and considering that the N-MC-C-derived GDE was proven to generate more H_2O_2 than the MC-C GDE in the absence of Fe^{2+} (Figure 5a), a greater $^{\bullet}OH$ production can be inferred. This should entail a faster water decontamination, as will be discussed later. The result obtained in these EF systems is in good agreement with that previously reported with a commercial GDE in an analogous solution (< 10 mM H_2O_2 at 30 mA/cm^2).[79] Similar experiments were made exposing solutions with the same composition to UVA photons (PEF conditions), which caused an additional reduction in the content of the oxidant accumulated at each electrolysis time until reaching ~4.6 mM H_2O_2 at 360 min (Figure 5b). This is explained by the occurrence of photo-

513 Fenton reaction (3), with optimum λ = 360 nm. The continuous Fe^{2+} photo-induced regeneration
514 sustained the Fenton's reaction (2), which otherwise would be mitigated due to the gradual
515 conversion of Fe^{2+} into the much less active species $[Fe(OH)]^{2+}$ (i.e., the main Fe(III) species at
516 pH 3.0).[5]

517 The current efficiencies for all the trials depicted in Figure 5a and 5b, determined from Eq.
518 (4), are illustrated in Figure S4a and S4b, respectively. In all cases, a loss of efficiency over time
519 can be observed, in agreement with the progressively lower H_2O_2 accumulation rate (i.e., the
520 curvature appearance after some minutes in Figure 5 owing to parasitic reactions). In the absence
521 of Fe^{2+} (Figure S4a), the maximum efficiency of ~40% (reasonably good taking into account that
522 the cell was undivided) corresponded to the treatment with N-MC-C at 10 mA/cm^2. Worth
523 noticing, upon increase to 30 mA/cm^2 the efficiency profile was very similar, which is interesting
524 in practice to promote a faster degradation. Therefore, this current density was selected as optimum
525 for subsequent trials. When the current density was then doubled, the efficiency was almost halved,
526 confirming the detrimental enhancement of parasitic destruction reactions (i.e., cathodic and
527 anodic phenomena mentioned before). All the treatments with the MC-C-derived GDE were much
528 less efficient (< 25% during all the electrolysis). As expected from the practically overlapping
529 H_2O_2 profiles found in EF and PEF (Figure 5a), Figure S4b evidences similar trends for the
530 corresponding current efficiencies (always lower than 20%), with slightly higher values in EF
531 assays.

532 **Degradation of acebutolol using GDEs prepared with the synthesized catalysts.** For the
533 dual purpose of assessing the viability of the new GDEs to foster the degradation of organic
534 pollutants and confirming the superiority of N-MC-C electrocatalyst, solutions containing 0.046
535 mM of the β-blocker acebutolol and 0.050 M Na_2SO_4 at pH 3.0 were electrolyzed at the optimized
536 current density (30 mA/cm^2). In Figure 6a, the drug concentration decays under electro-oxidation
537 (EO-H_2O_2) conditions with each GDE. The degradation was quite slow in both cases, ending in

538 modest removals of 35% and 51% at 180 min using the MC-C- and N-MC-C-derived GDE,
539 respectively. Since H_2O_2 behaves as a rather mild oxidant in front of aromatic structures like that
540 exhibited by acebutolol, within the concentration ranges as that discussed from Figure 5a,[6] the
541 partial drug disappearance can be attributed to the action of hydroxyl radicals M(•OH) formed on
542 the anode (M) surface from reaction (13).[40,48] The data could not be fitted well considering a simple
543 kinetic model, thus suggesting a larger complexity due to the influence of reaction products.

544 $$M + H_2O \rightarrow M(^{\bullet}OH) + H^+ + e^- \quad (13)$$

545 The degradation was drastically upgraded in the presence of 0.50 mM Fe^{2+} and UVA photons
546 under PEF conditions, as evidenced in Figure 6b. The use of the two DSA/GDE cells led to 97%
547 and 100% acebutolol removal in only 20 min using the MC-C and N-MC-C electrocatalyst,
548 respectively. Such significant acceleration of concentration decays was pre-eminently favored by
549 the generation of •OH upon fast decomposition of H_2O_2 via Fenton's reaction (2), which confirms
550 the explanation given on the time course of H_2O_2 (Figure 5b). The effective •OH production was
551 ensured by the continuous Fe(III) photoreduction from reaction (3), which yielded additional
552 amounts of •OH and regenerated the Fe^{2+}. The replacement of the RuO_2-based anode by BDD had
553 a positive influence on the destruction of the pollutant, being more evident in the system with N-
554 MC-C, since the complete disappearance was observed at 16 min. Using MC-C, almost no change
555 in degradation percentage (98%) was reached, but the initial concentration decay became quicker.
556 This is clear in the inset of Figure 6b, which depicts the excellent linear fitting ($R^2 > 0.990$)
557 resulting from a pseudo-first-order kinetic analysis of all decays of the main figure. The pseudo-
558 first-order rate constant (k_1) increased from 0.1748 to 0.2296 min^{-1} when the anode was changed
559 to BDD in the system with MC-C. Accordingly, higher k_1-values were determined using N-MC-
560 C, namely 0.2583 and 0.3258 min^{-1} with DSA and BDD, respectively. The enhancement achieved
561 with BDD anode is associated to the physisorbed nature of M(•OH) produced from reaction (13),
562 which makes the radicals more reactive with organic molecules approaching its surface.[48]

563 However, it is clear that the main factors affecting the drug degradation were those related with
564 the Fenton's reactivity, as can be deduced when comparing Figure 6a and 6b. Among such factors,
565 the benefit of the higher H_2O_2 electrogeneration with N-MC-C stands out.

566 The performance of our biomass-derived GDEs is comparable to that reported for GDEs
567 prepared with carbon cloth coated with commercial carbon black. For example, the treatment of
568 β-blocker atenolol in 0.050 M Na_2SO_4 at pH 3.0 by PEF at 16.7 mA/cm^2 allowed the total drug
569 removal in 30-35 min, with k_1 = 0.05 min^{-1}, thus being in the same order of magnitude.[80]

570 Figure 7 highlights the time course of normalized TOC content with electrolysis time during
571 the PEF assays of Figure 6b. Unlike that observed in the previous HPLC analysis, the effect of the
572 anode nature was crucial to upgrade the mineralization of the solutions, which initially contained
573 10 mg/L TOC. Partial TOC abatements were obtained with DSA, attaining 71% and 76% at 360
574 min using MC-C and N-MC-C, respectively. A much greater decontamination was feasible upon
575 use of BDD anode, with final values of 91% and 97%. In all these systems, the effective generation
576 of $^{\bullet}$OH in the bulk sustained by reaction (3) undoubtedly contributed to the gradual degradation of
577 reaction products. However, this was insufficient because it is known that the aromatic molecules
578 are transformed into very refractory aliphatic products and their complexes with Fe(III) that resist
579 quite well the attack of $^{\bullet}$OH.[3,4] Therefore, UVA photons played an additional role, allowing the
580 photodecarboxylation of such stable complexes:

581 $$[Fe(OOCR)]^{2+} + h\nu \rightarrow Fe^{2+} + R^{\bullet} + CO_2 \quad (14)$$

582 As inferred from both PEF trials with DSA, the degradation power of $^{\bullet}$OH and UVA light was
583 still limited and hence, M($^{\bullet}$OH) formed at BDD favored the electrocatalytic destruction of the
584 refractory molecules. As a result, the combination of the most effective anode and cathode yielded
585 the greater mineralization. Note that TOC decays reported for acebutolol solutions through other
586 advanced oxidation processes were lower, as in the case of photocatalysis with TiO_2 with 75%
587 mineralization at 240 min.[81]

588 The following overall mineralization reaction can be proposed, based on the determination of
589 inorganic ions discussed below:[5]

590 $$C_{18}H_{28}N_2O_4 + 32H_2O \rightarrow 18CO_2 + 2NH_4^+ + 84H^+ + 86e^- \quad (15)$$

591 From Eq. (5), in which the total number of electrons involved was n = 86, the MCE values
592 calculated at a given electrolysis time for the assays of Figure 7 are represented in Figure S5a. The
593 most efficient process was PEF with the BDD/GDE cell using N-MC-C, in agreement with the
594 effective TOC removal in that system. Nonetheless, the fact that the maximum MCE was < 15%
595 reflects the high refractoriness of the pollutant and its derivatives. As the treatments progressed, a
596 loss of efficiency was observed, meaning that the organic structures and complexes formed were
597 more resistant to $^{\bullet}$OH, M($^{\bullet}$OH) and UVA photons than the target pollutant and its primary
598 intermediates. In addition, the side reactions that wasted the radicals and photons occurred to a
599 greater extent as the number of available organic molecules decreased. These two phenomena with
600 negative impact on the process efficiency were also detrimental in terms of energy consumption.
601 The EC_{TOC} values calculated from Eq. (6) and represented in Figure 6b were higher in trials with
602 BDD, which is mainly explained by the much greater E_{cell} as compared to those with the RuO_2-
603 based anode (15.5 vs 8.0 V, regardless of the GDE). Note that these energy consumptions are
604 purely electrolytic. If the lamp consumption is added (i.e., the term $E_{cell}I$ in Eq. (6) is replaced by
605 the lamp power to determine $(EC)_{photo}$),[82] the EC_{TOC} values increase up to ~30 and ~36 kWh / g
606 TOC using BDD and DSA, respectively. In practice, natural sunlight can be used instead artificial
607 UVA light, thus avoiding the large contribution of $(EC)_{photo}$.

608 In Figure 8a-d, the SEM images of GDEs prepared with both chitosan-based electrocatalysts
609 can be seen at two different magnifications. A good surface coverage of carbon cloth was obtained
610 with MC-C and N-MC-C, with no evidence of exposed carbon fibers. This is attributed to the good
611 spraying procedure, giving rise to several layers, followed by hot pressing. Some gaps can be
612 appreciated, which are better identified at the highest magnification (Figure 8b and 8d). These

613 macropores favored the mass transport rate of O_2 toward the catalytic sites.[5] Amorphous particles
614 with dimensions of some microns appear in both types of GDE, as is typical for C-PTFE GDEs.
615 Some of them formed clusters wrapped around the fibers (Figure 8b). PTFE, recognized as the
616 white spots, was spread over the surface, conferring sufficient hydrophobicity to the materials.
617 Note that no flooding of the GDEs was observed during the trials of this work. The GDEs used in
618 PEF treatments with DSA described in Figure 7 were collected at the end of the electrolyses. The
619 corresponding SEM analysis (Figure 8a'-d') at the same magnifications mainly show smoother
620 surfaces without clear distinction of carbon particles and, more important, the obvious presence of
621 uncoated or partially coated fibers. This phenomenon was more evident in the cathode prepared
622 with MC-C, which can be directly explained from its aforementioned lower stability. Oxygen gas
623 is forced through its compact structure, causing a partial disintegration. However, this did not
624 impede to reuse all the GDEs for several consecutive runs without any substantial loss of
625 performance related to H_2O_2 production and degradation ability.

626 **Reaction products identified during the PEF treatment of acebutolol solutions.** In the
627 previous subsection, the TOC-time and MCE-time profiles have been justified on the basis of the
628 different reactivity of the reaction products. To demonstrate this, a 0.046 mM acebutolol solution
629 with 0.050 M Na_2SO_4 and 0.50 mM Fe^{2+} at pH 3.0 was treated by PEF for 60 min, using a cell
630 with the RuO_2-based anode connected to a GDE made with N-MC-C catalyst, at 30 mA/cm^2.
631 Samples collected at 10 and 60 min and analyzed by GC/MS revealed the presence of six aromatic
632 and three nitrogenated aliphatic compounds, whose characteristics are summarized in Table S3. In
633 Figure 9, the generation of these molecules is proposed considering the modification of parts R1,
634 R2, R3 and R4 distinguished in acebutolol. Some authors detected a product similar to **2**, but
635 hydroxylated in C1 position, when acebutolol solutions were treated by droplet-assisted
636 heterogeneous EF.[83] They also identified a structure close to **6** but keeping R1, and another one
637 like **7** but non-hydroxylated.

638 Most of these nine products were expected to be gradually hydroxylated.[5] Therefore, the
639 evolution of the concentration of short-chain linear carboxylic acids during the same kind of PEF
640 treatment was investigated. Figure 10 evidences the trends of oxalic acid, whose peak was found
641 at retention time of 7.0 min, and oxamic acid, which appeared at 9.8 min. The former attained a
642 maximum concentration of 1.75 mg/L at 30 min, quickly decaying to finally disappear at 120 min.
643 Oxalic acid is a typical end organic product from aromatic pollutants, which is the reason that
644 explains that it was the main accumulated carboxylic acid.[51] The high photoactivity of its
645 complexed form under UVA light according to reaction (14) justifies its total degradation in PEF.
646 In contrast, oxamic was only formed from larger N-structures, reaching a lower content of 1.05
647 mg/L at 60 min. Moreover, since it formed much less photoactive complexes,[51] it persisted in the
648 solution during the entire electrolysis. The presence of both acids as acebutolol is degraded has
649 also been reported elsewhere.[83]

650 The inorganic ions generated in PEF treatment from the heteroatoms contained in the drug
651 were determined as well. A more concentrated acebutolol solution (i.e., 0.092 mM) was employed
652 in order to facilitate the quantification. Neither nitrite nor nitrate were identified, being NH_4^+ the
653 only dissolved nitrogenated ion detected, thus corroborating the validity of mineralization reaction
654 (15). The ammonium content increased all the time, as the organic N-structures were degraded,
655 attaining 1.43 mg/L at 360 min. This cation was also the main nitrogenated ion found during the
656 degradation of other N-aromatic pollutants by Fenton-based electrochemical processes.[70] A
657 nitrogen balance after normalizing the acebutolol content suggests that the treated solutions
658 contained ~50% of initial dissolved nitrogen, most of it corresponding to NH_4^+. This means that
659 some N-containing gases were released during the PEF treatment of acebutolol.

CONCLUSIONS

This work reports the successful synthesis and characterization of a potentially cheaper and more eco-friendly material to electrogenerate sufficient amounts of H_2O_2 for its direct application in Fenton-based electrochemical water treatment. Chitosan was considered as raw material for the preparation of N-doped carbon. It was observed that the addition of 1,10-phenathroline as co-reactant during the pyrolysis treatments conferred better textural properties and surface N-functionalization than the sole chitosan. LSV at RRDE highlighted the higher catalytic activity of N-MC-C, in terms of $E_{1/2}$. GDEs prepared with N-MC-C showed H_2O_2 yields in the same range attainable with commercial GDE. The degradation of 0.046 mM acebutolol solutions was made with the N-MC-C-derived GDE coupled to a RuO_2-based anode in an electrochemical cell at pH 3.0. The PEF assays in such cell resulted in a fast and complete drug removal. The use of BDD instead of DSA had a positive influence on the decontamination, since the almost complete TOC removal was achieved at the end of the electrolysis. GC/MS analysis clarified the main aromatic and aliphatic products formed during the mineralization process. Short-chain linear carboxylic acids such as oxalic and oxamic were generated as final organic compounds, whereas NH_4^+ was the main ion.

ASSOCIATED CONTENT

Supporting Information (SI)

Figures S1-S5.

Tables S1-S3.

The Supporting Information is available free of charge on the ACS Publications website.

ACKNOWLEDGMENTS

The authors kindly acknowledge support from projects DOR2018 (University of Padova), CTQ2016-78616-R (AEI/FEDER, EU) and PID2019-109291RB-I00 (AEI, Spain), as well as the PhD scholarship awarded to Yanyu Zhang (State Scholarship Fund, CSC, China).

REFERENCES

(1) Guo, X.; Lin, S.; Gu, J.; Zhang, S.; Chen, Z.; Huang, S. Simultaneously achieving high activity and selectivity toward two-electron O_2 electroreduction: The power of single-atom catalysts. *ACS Catal.* **2019**, *9*, 11042-11054; DOI 10.1021/acscatal.9b02778.

(2) Rocha, R. S.; Silva, F. L.; Valim, R. B.; Barros, W. R. P.; Steter, J. R.; Bertazzoli, R.; Lanza, M. R. V. Effect of Fe^{2+} on the degradation of the pesticide profenofos by electrogenerated H_2O_2. *J. Electroanal. Chem.* **2016**, *783*, 100-105; DOI 10.1016/j.jelechem.2016.11.038.

(3) Ye, Z.; Guelfi, D. R. V.; Álvarez, G.; Alcaide, F.; Brillas, E.; Sirés, I. Enhanced electrocatalytic production of H_2O_2 at Co-based air-diffusion cathodes for the photoelectro-Fenton treatment of bronopol. *Appl. Catal. B: Environ.* **2019**, *247*, 191-199; DOI 10.1016/j.apcatb.2019.01.029.

(4) Alcaide, F.; Álvarez, G.; Guelfi, D. R. V.; Brillas, E.; Sirés, I. A stable CoSP/MWCNTs air-diffusion cathode for the photoelectro-Fenton degradation of organic pollutants at pre-pilot scale. *Chem. Eng. J.* **2020**, *379*, 122417; DOI 10.1016/j.cej.2019.122417.

(5) Brillas, E.; Sirés, I.; Oturan, M. A. Electro-Fenton process and related electrochemical technologies based on Fenton's reaction chemistry. *Chem. Rev.* **2009**, *109*, 6570-6631; DOI 10.1021/cr900136g.

(6) Borghei, M.; Lehtonen, J.; Liu, L.; Rojas, O. J. Advanced biomass-derived electrocatalysts for the oxygen reduction reaction. *Adv. Mater.* **2018**, *30*, 1703691; DOI 10.1002/adma.201703691.

(7) Chai, G. -L.; Hou, Z.; Ikeda, T.; Terakura, K. Two-electron oxygen reduction on carbon materials catalysts: Mechanisms and active sites. *J. Phys. Chem. C* **2017**, *121*, 14524-14533; DOI 10.1021/acs.jpcc.7b04959.

(8) Chen, S.; Chen, Z.; Siahrostami, S.; Roy Kim, T.; Nordlund, D.; Sokaras, D.; Nowak, S.; To, J. W. F.; Higgins, D.; Sinclair, R.; Nørskov, J. K.; Jaramillo, T. F.; Bao, Z. Defective carbon-based materials for the electrochemical synthesis of hydrogen peroxide. *ACS Sustain. Chem. Eng.* **2018**, *6*, 311-317; DOI 10.1021/acssuschemeng.7b02517.

(9) Čolić, V.; Yang, S.; Révay, Z.; Stephens, I. E. L.; Chorkendorff, I. Carbon catalysts for electrochemical hydrogen peroxide production in acidic media. *Electrochim. Acta* **2018**, *272*, 192-202; DOI 10.1016/j.electacta.2018.03.170.

(10) Sun, Y.; Sinev, I.; Ju, W.; Bergmann, A.; Dresp, S.; Kühl, S.; Spöri, C.; Schmies, H.; Wang, H.; Bernsmeier, D.; Paul, B.; Schmack, R.; Kraehnert, R.; Roldan Cuenya, B.; Strasser, P. Efficient electrochemical hydrogen peroxide production from molecular oxygen on nitrogen-doped mesoporous carbon catalysts. *ACS Catal.* **2018**, *8*, 2844-2856; DOI 10.1021/acscatal.7b03464.

(11) Choi, C. H.; Kim, M.; Kwon, H. C.; Cho, S. J.; Yun, S.; Kim, H. T.; Mayrhofer, K. J. J.; Kim, H.; Choi, M. Tuning selectivity of electrochemical reactions by atomically dispersed platinum catalyst. *Nature Comm.* **2016**, *7*, 10922; DOI 10.1038/ncomms10922.

(12) Perazzolo, V.; Durante, C.; Pilot, R.; Paduano, A.; Zheng, J.; Rizzi, G. A.; Martucci, A.; Granozzi, G.; Gennaro, A. Nitrogen and sulfur doped mesoporous carbon as metal-free electrocatalysts for the in situ production of hydrogen peroxide. *Carbon* **2015**, *95*, 949-963; DOI 10.1016/j.carbon.2015.09.002.

(13) Perazzolo, V.; Durante, C.; Gennaro, A. Nitrogen and sulfur doped mesoporous carbon cathodes for water treatment. *J. Electroanal. Chem.* **2016**, *782*, 264-269; DOI 10.1016/j.jelechem.2016.10.037.

730 (14) Roldán, L.; Truong-Phuoc, L.; Ansón-Casaos, A.; Pham-Huu, C.; García-Bordejé, E.
731 Mesoporous carbon doped with N,S heteroatoms prepared by one-pot auto-assembly of molecular
732 precursor for electrocatalytic hydrogen peroxide synthesis. *Catal. Today* **2018**, *301*, 2-10; DOI
733 10.1016/j.cattod.2016.12.020.
734 (15) Favaro, M.; Perini, L.; Agnoli, S.; Durante, C.; Granozzi, G.; Gennaro, A.
735 Electrochemical behavior of N and Ar implanted highly oriented pyrolytic graphite substrates and
736 activity toward oxygen reduction reaction. *Electrochim. Acta* **2013**, *88*, 477-487; DOI
737 10.1016/j.electacta.2012.10.100.
738 (16) Xing, T.; Sunarso, J.; Yang, W.; Yin, Y.; Glushenkov, A. M.; Li, L. H.; Howlett, P.
739 C.; Chen, Y. Ball milling: a green mechanochemical approach for synthesis of nitrogen doped
740 carbon nanoparticles. *Nanoscale* **2013**, *5*, 7970-7976. DOI 10.1039/c3nr02328a
741 (17) Tuci, G.; Zafferoni, C.; Rossin, A.; Milella, A.; Luconi, L.; Innocenti, M.; Truong
742 Phuoc, L.; Duong-Viet, C.; Pham-Huu, C.; Giambastiani, G. Chemically functionalized carbon
743 nanotubes with pyridine groups as easily tunable N-decorated nanomaterials for the oxygen
744 reduction reaction in alkaline medium. *Chem. Mater.* **2014**, *26*, 3460-3470; DOI
745 10.1021/cm500805c.
746 (18) Kabir, S.; Artyushkova, K.; Serov, A.; Atanassov, P. Role of nitrogen moieties in
747 N‐doped 3D-graphene nanosheets for oxygen electroreduction in acidic and alkaline media. ACS
748 Appl. Mater. Interfaces **2018**, *10*, 11623-11632; DOI 10.1021/acsami.7b18651.
749 (19) Brandiele, R.; Durante, C.; Zerbetto, M.; Vicentini, N.; Kosmala, T.; Badocco, D.;
750 Pastore, P.; Rizzi, G. A.; Isse, A. A.; Gennaro, A. Probing the correlation between Pt-support
751 interaction and oxygen reduction reaction activity in mesoporous carbon materials modified with
752 Pt-N active sites. *Electrochim. Acta* **2018**, *277*, 287-300; DOI 10.1016/j.electacta.2018.04.182.

(20) Yang, W.; Zhou, M.; Liang, L. Highly efficient in-situ metal-free electrochemical advanced oxidation process using graphite felt modified with N-doped graphene. *Chem. Eng. J.* **2018**, *338*, 700-708; DOI 10.1016/j.cej.2018.01.013.

(21) Yang, W.; Zhou, M.; Oturan, N.; Li, Y.; Su, P.; Oturan, M. A. Enhanced activation of hydrogen peroxide using nitrogen doped graphene for effective removal of herbicide 2,4-D from water by iron-free electrochemical advanced oxidation. *Electrochim. Acta* **2019**, *297*, 582-592; DOI 10.1016/j.electacta.2018.11.196.

(22) Iglesias, D.; Giuliani, A.; Melchionna, M.; Marchesan, S.; Criado, A.; Nasi, L.; Bevilacqua, M.; Tavagnacco, C.; Vizza, F.; Prato, M.; Fornasiero, P. N-doped graphitized carbon nanohorns as a forefront electrocatalyst in highly selective O_2 reduction to H_2O_2. *Chem* **2018**, *4*, 106-123; DOI 10.1016/j.chempr.2017.10.013.

(23) Bi, Z.; Kong, Q.; Cao, Y.; Sun, G.; Su, F.; Wei, X.; Li, X.; Ahmad, A.; Xie, L.; Chen, C. -M. Biomass-derived porous carbon materials with different dimensions for supercapacitor electrodes: a review. *J. Mater. Chem. A* **2019**, *7*, 16028-16045; DOI 10.1039/C9TA04436A.

(24) Antolini, E. Nitrogen-doped carbons by sustainable N- and C-containing natural resources as nonprecious catalysts and catalyst supports for low temperature fuel cells. *Renew. Sustain. Energy Rev.* **2016**, *58*, 34-51; DOI 10.1016/j.rser.2015.12.330.

(25) Liu, F.; Liu, L.; Li, X.; Zeng, J.; Du, L.; Liao, S. Nitrogen self-doped carbon nanoparticles derived from spiral seaweeds for oxygen reduction reaction. *RSC Adv.* **2016**, *6*, 27535-27541; DOI 10.1039/C5RA27499K.

(26) Chen, Y.; Wang, M.; Tian, M.; Zhu, Y.; Wei, X.; Jiang, T.; Gao, S. An innovative electro-fenton degradation system self-powered by triboelectric nanogenerator using biomass-derived carbon materials as cathode catalyst. *Nano Energy* **2017**, *42*, 314-321; DOI 10.1016/j.nanoen.2017.10.060.

(27) Yang, Y.; He, F.; Shen, Y.; Chen, X.; Mei, H.; Liu, S.; Zhang, Y. A biomass derived N/C-catalyst for the electrochemical production of hydrogen peroxide. *Chem. Commun.* **2017**, *53*, 9994-9997; DOI 10.1039/c7cc04819j.

(28) Daniel, G.; Foltran, E.; Brandiele, R.; Nodari, L.; Pilot, R.; Menna, E.; Rizzi, G. A.; Isse, A. A.; Durante, C.; Gennaro, A. Platinum-free electrocatalysts for oxygen reduction reaction: Fe-N_x modified mesoporous carbon prepared from biosources. *J. Power Sources* **2018**, *402*, 434-446; DOI 10.1016/j.jpowsour.2018.09.060.

(29) Kim, M. -J.; Park, J. E.; Kim, S.; Lim, M. S.; Jin, A.; Kim, O. -H.; Kim, M. J.; Lee, K. -S.; Kim, J.; Kim, S. -S.; Cho, Y. -H.; Sung, Y. -E. Biomass-derived air cathode materials: Pore-controlled S,N-co-doped carbon for fuel cells and metal–air batteries. *ACS Catal.* **2019**, *9*, 3389-3398; DOI 10.1021/acscatal.8b03730.

(30) Tian, M.; Zhu, Y.; Zhang, D.; Wang, M.; Chen, Y.; Yang, Y.; Gao, S. Pyrrolic-nitrogen-rich biomass-derived catalyst for sustainable degradation of organic pollutant *via* a self-powered electro-Fenton process. *Nano Energy* **2019**, *64*, 103940; DOI 10.1016/j.nanoen.2019.103940.

(31) Wu, X.; Chen, K.; Lin, Z.; Zhang, Y.; Meng, H. Nitrogen doped graphitic carbon from biomass as non noble metal catalyst for oxygen reduction reaction. *Mater. Today Energy* **2019**, *13*, 100-108; DOI 10.1016/j.mtener.2019.05.004.

(32) Jia, N.; Yang, T.; Shi, S.; Chen, X.; An, Z.; Chen, Y.; Yin, S.; Chen, P. N,F-codoped carbon nanocages: An efficient electrocatalyst for hydrogen peroxide electroproduction in alkaline and acidic solutions. *ACS Sustain. Chem. Eng.* **2020**, *8*, 2883-2891; DOI 10.1021/acssuschemeng.9b07047.

(33) Le, T. X. H.; Bechelany, M.; Lacour, S.; Oturan, N.; Oturan, M. A.; Cretin, M. High removal efficiency of dye pollutants by electron-Fenton process using a graphene based cathode. *Carbon* **2015**, *94*, 1003-1011; DOI 10.1016/j.carbon.2015.07.086.

802 (34) Castañeda, L. F.; Walsh, F. C.; Nava, J. L.; Ponce de León, C. Graphite felt as a
803 versatile electrode material: Properties, reaction environment, performance and applications.
804 *Electrochim. Acta* **2017**, *258*, 1115-1139; DOI 10.1016/j.electacta.2017.11.165.
805 (35) Yu, F.; Chen, Y.; Ma, H. Ultrahigh yield of hydrogen peroxide and effective diclofenac
806 degradation on a graphite felt cathode loaded with CNTs and carbon black: an electro-generation
807 mechanism and a degradation pathway. *New J. Chem.* **2018**, *42*, 4485-4494; DOI
808 10.1039/C7NJ04925K.
809 (36) Ye, Z.; Brillas, E.; Centellas, F.; Cabot, P. L.; Sirés, I. Electro-Fenton process at mild
810 pH using Fe(III)-EDDS as soluble catalyst and carbon felt as cathode. *Appl. Catal. B: Environ.*
811 **2019**, *257*, 117907; DOI 10.1016/j.apcatb.2019.117907.
812 (37) Scialdone, O.; Galia, A.; Gattuso, C.; Sabatino, S.; Schiavo, B. Effect of air pressure
813 on the electro-generation of H_2O_2 and the abatement of organic pollutants in water by electro-
814 Fenton process. *Electrochim. Acta* **2015**, *182*, 775-780; DOI 10.1016/j.electacta.2015.09.109.
815 (38) Zhou, W.; Meng, X.; Gao, J.; Alshawabkeh, A. N. Hydrogen peroxide generation from
816 O_2 electroreduction for environmental remediation: A state-of-the-art review. *Chemosphere* **2019**,
817 *225*, 588-607; DOI 10.1016/j.chemosphere.2019.03.042.
818 (39) Coria, G.; Pérez, T.; Sirés, I.; Brillas, E.; Nava, J. L. Abatement of the antibiotic
819 levofloxacin in a solar photoelectro-Fenton flow plant: Modeling the dissolved organic carbon
820 concentration-time relationship. *Chemosphere* **2018**, *198*, 174-181; DOI
821 10.1016/j.chemosphere.2018.01.112.
822 (40) Galia, A.; Lanzalaco, S.; Sabatino, M. A.; Dispenza, C.; Scialdone, O.; Sirés, I.
823 Crosslinking of poly(vinylpyrrolidone) activated by electrogenerated hydroxyl radicals: a first step
824 towards a simple and cheap synthetic route of nanogel vectors. *Electrochem. Commun*. **2016**, *62*,
825 64-68; DOI 10.1016/j.elecom.2015.12.005.

(41) Lanzalaco, S.; Sirés, I.; Sabatino, M. A.; Dispenza, C.; Scialdone, O.; Galia, A. Synthesis of polymer nanogels by electro-Fenton process: investigation of the effect of main operation parameters. *Electrochim. Acta*. **2017**, *246*, 812-822; DOI 10.1016/j.electacta.2017.06.097.

(42) Ding, P.; Cui, L.; Li, D.; Jing, W. Innovative dual-compartment flow reactor coupled with a gas diffusion electrode for in situ generation of H_2O_2. *Ind. Eng. Chem. Res.* **2019**, *58*, 6925-6932; DOI 10.1021/acs.iecr.9b00358.

(43) Zhang, H.; Li, Y.; Zhao, Y.; Li, G.; Zhang, F. Carbon black oxidized by air calcination for enhanced H_2O_2 generation and effective organics degradation. *ACS Appl. Mater. Interfaces* **2019**, *11*, 27846-27853; DOI 10.1021/acsami.9b07765.

(44) Zhang, Q.; Zhou, M.; Ren, G.; Li, Y.; Li, Y.; Du, X. Highly efficient electrosynthesis of hydrogen peroxide on a superhydrophobic three-phase interface by natural air diffusion. *Nature Commun.* **2020**, *11*, 1731; DOI 10.1038/s41467-020-15597-y.

(45) Gendel, Y.; Roth, H.; Rommerskirchen, A.; David, O.; Wessling, M. A microtubular all CNT gas diffusion electrode. *Electrochem. Commun.* **2014**, *46*, 44-47; DOI 10.1016/j.elecom.2014.06.006.

(46) Mousset, E.; Ko, Z. T.; Syafiq, M.; Wang, Z.; Lefebvre, O. Electrocatalytic activity enhancement of a graphene ink-coated carbon cloth cathode for oxidative treatment. *Electrochim. Acta* **2016**, *222*, 1628-1641; DOI 10.1016/j.electacta.2016.11.151.

(47) Kolyagin, G. A.; Kornienko, G. V.; Kornienko, V. L.; Ponomarenko, I. V. Electrochemical reduction of oxygen to hydrogen peroxide in a gas-diffusion electrode based on mesoporous carbon. *Russ. J. Appl. Chem.* **2017**, *90*, 1143-1147; DOI 10.1134/S1070427217070187.

(48) Martínez-Huitle, C. A.; Rodrigo, M. A.; Sirés, I.; Scialdone, O. Single and coupled electrochemical processes and reactors for the abatement of organic water pollutants: a critical review. *Chem. Rev.* **2015**, *115* (24), 13362-13407; DOI 10.1007/s11356-014-2783-1.

(49) Yang, W.; Zhou, M.; Oturan, N.; Li, Y.; Oturan, M. A. Electrocatalytic destruction of pharmaceutical imatinib by electro-Fenton process with graphene-based cathode. *Electrochim. Acta* **2019**, *305*, 285-294; DOI 10.1016/j.electacta.2019.03.067.

(50) Ye, Z.; Padilla, J. A.; Xuriguera, E.; Beltran, J. L.; Alcaide, F.; Brillas, E.; Sirés, I. A highly stable metal-organic framework-engineered FeS_2/C nanocatalyst for heterogeneous electro-Fenton treatment: Validation in wastewater at mild pH. *Environ. Sci. Technol.* **2020**, *54*, 4664-4674; DOI 10.1016/j.electacta.2019.03.067.

(51) Zhou, M.; Oturan, M. A.; Sirés, I. Electro-Fenton Process: New Trends and Scale-Up, *Springer Nature*, Singapore, **2018**.

(52) Brillas, E. A review on the photoelectro-Fenton process as efficient electrochemical advanced oxidation for wastewater remediation. Treatment with UV light, sunlight, and coupling with conventional and other photo-assisted advanced technologies. *Chemosphere* **2020**, *250*, 126198; DOI 10.1016/j.chemosphere.2020.126198.

(53) Wen, Z.; Wang, A.; Zhang, Y.; Ren, S.; Tian, X.; Li, J. Mineralization of cefoperazone in acid medium by the microwave discharge electrodeless lamp irradiated photoelectro-Fenton using a RuO_2/Ti or boron-doped diamond anode. *J. Hazard. Mater.* **2019**, *374*, 186-194; DOI 10.1016/j.jhazmat.2019.03.124.

(54) Zhang, Y.; Wang, A.; Ren, S.; Wen, Z.; Tian, X.; Li, D.; Li, J. Effect of surface properties of activated carbon fiber cathode on mineralization of antibiotic cefalexin by electro-Fenton and photoelectro-Fenton treatments: Mineralization, kinetics and oxidation products. *Chemosphere* **2019**, *221*, 423-432; DOI 10.1016/j.chemosphere.2019.01.016.

(55) Liu, T.; Wang, K.; Song, S.; Brouzgou, A.; Tsiakaras, P.; Wang, Y. New electro-Fenton gas diffusion cathode based on nitrogen-doped graphene@carbon nanotube composite materials. *Electrochim. Acta* **2016**, *194*, 228-238; DOI 10.1016/j.electacta.2015.12.185.

(56) Zhu, Y.; Qiu, S.; Deng, F.; Ma, F.; Zheng, Y. Degradation of sulfathiazole by electro-Fenton using a nitrogen-doped cathode and a BDD anode: Insight into the H_2O_2 generation and radical oxidation. *Sci. Total Environ.* **2020**, *722*, 137853; DOI 10.1016/j.scitotenv.2020.137853.

(57) Liao, M. -J.; Wang, Y. -L.; Li, S. -S.; Li, J. -F.; Chen, P. Electrocatalyst derived from abundant biomass and its excellent activity for in situ H_2O_2 production. *ChemElectroChem* **2019**, *6*, 4877-4884; DOI 10.1002/celc.201901321.

(58) Pujol, A. A.; León, I; Cárdenas, J.; Sepúlveda-Guzmán, S.; Manríquez, J.; Sirés, I.; Bustos, E. Degradation of phenols by heterogeneous electro-Fenton with a Fe_3O_4-chitosan composite and a boron-doped diamond anode. *Electrochim. Acta* **2020**, *337*, 135784; DOI 10.1016/j.electacta.2020.135784.

(59) El Knidri, H.; Belaabed, R.; Addaou, A.; Laajeb, A.; Lahsini, A. Extraction, chemical modification and characterization of chitin and chitosan. *Int. J. Biol. Macromol.* **2018**, *120A*, 1181-1189; DOI 10.1016/j.ijbiomac.2018.08.139.

(60) Majeti, N. V.; Kumar, R. A review of chitin and chitosan applications. *React. Funct. Polym.* **2000**, *46*, 1-27; DOI 10.1016/S1381-5148(00)00038-9.

(61) Kümmerer, K.; Dionysiou, D. D.; Olsson, O.; Fatta-Kassinos, D. A path to clean water. *Science* **2018**, *361*(6399), 222-224; DOI 10.1126/science.aau2405.

(62) Varga, R.; Somogyvári, I.; Eke, Z.; Torkos, K. Determination of antihypertensive and anti-ulcer agents from surface water with solid-phase extraction–liquid chromatography–electrospray ionization tandem mass spectrometry. *Chemosphere* **2011**, *83*, 1447-1454; DOI 10.1016/j.talanta.2010.11.030.

(63) Daneshvar, A.; Svanfelt, J.; Kronberg, L.; Prévost, M.; Weyhenmeyer, G. A. Seasonal variations in the occurrence and fate of basic and neutral pharmaceuticals in a Swedish river-lake system. *Chemosphere* **2010**, *80*, 301-309; DOI 10.1016/j.chemosphere.2010.03.060.

(64) Fraysse, B.; Garric, J. Prediction and experimental validation of acute toxicity of β-blockers in *Ceriodaphnia dubia*. *Environ. Toxicol.* **2005**, *24*, 2470-2476; DOI 10.1897/04-541r.1.

(65) Blake, S. C.; D, M.; Daniel, B. S.; S, M. B. B.; D, F. A. C. Cutaneous lupus erythematosus: A review of the literature. *Int. J. Women. Dermatol.* **2019**, *5*, 320-329; DOI 10.1016/j.ijwd.2019.07.004.

(66) Fan, M.; Hu, Q.; Shen, K. Preparation and structure of chitosan soluble in wide pH range. *Carbohydr. Polym.* **2009**, *78*, 66-71; DOI 10.1016/j.carbpol.2009.03.031.

(67) Nie, J.; Wang, Z.; Hu, Q. Difference between chitosan hydrogels via alkaline and acidic solvent systems. *Sci. Rep.* **2016**, *6*, 36053; DOI 10.1038/srep36053.

(68) Li, P.; Zhao, J.; Chen, Y.; Cheng, B.; Yu, Z.; Zhao, Y.; Yan, X.; Tong, Z.; Jin, S. Preparation and characterization of chitosan physical hydrogels with enhanced mechanical and antibacterial properties. *Carbohydr. Polym.* **2017**, *157*, 1383-1392; DOI 10.1016/j.carbpol.2016.11.016.

(69) Brandiele, R.; Durante, C.; Grądzka, E.; Rizzi, G. A.; Zheng, J.; Badocco, D.; Centomo, P.; Pastore, P.; Granozzi, G.; Gennaro, A. One step forward to a scalable synthesis of platinum–yttrium alloy nanoparticles on mesoporous carbon for the oxygen reduction reaction. *J. Mater. Chem. A* **2016**, *4*, 12232-12240; DOI 10.1039/C6TA04498K.

(70) Thiam, A.; Salazar, R.; Brillas, E.; Sirés, I. Electrochemical advanced oxidation of carbofuran in aqueous sulfate and/or chloride media using a flow cell with a RuO_2-based anode and an air diffusion cathode at pre-pilot scale. *Chem. Eng. J.* **2018**, *335*, 133-144; DOI 10.1016/j.cej.2017.10.137.

(71) Thommes, M.; Kaneko, K.; Neimark, A. V.; Olivier, J. P.; Rodriguez-Reinoso, F.; Rouquerol, J.; Sing, K. S. W. Physisorption of gases, with special reference to the evaluation of surface area and pore size distribution (IUPAC Technical Report). *Pure Appl. Chem.* **2015**, *87*, 1051-1069; DOI 10.1515/pac-2014-1117.

(72**)** Trevisanello, E.; De Bon, F.; Daniel, G.; Lorandi, F.; Durante, C.; Isse, A. A.; Gennaro, A. Electrochemically mediated atom transfer radical polymerization of acrylonitrile and poly(acrylonitrile-*b*-butyl acrylate) copolymer as a precursor for N-doped mesoporous carbons. *Electrochim. Acta* **2018**, *285*, 344-354; DOI 10.1016/j.electacta.2018.07.209.

(73) Brandiele, R.; Zerbetto, M.; Dalconi, M. C.; Rizzi, G. A.; Isse, A. A.; Durante, C.; Gennaro, A. Mesoporous carbon with different density of thiophenic-like functional groups and their effect on oxygen reduction. *ChemSusChem* **2019**, *12*, 4229-4239; DOI 10.1002/cssc.201901568.

(74) Brandiele, R.; Poli, F.; Picelli, L.; Pilot, R.; Rizzi, G. A.; Soavi, F.; Durante, C. Nitrogen doped mesoporous carbon electrodes prepared from templating propylamine functionalized silica. *ChemElectroChem* **2020**, *92*, 455-459. DOI 10.1002/celc.202000098.

(75) Bezerra, C. W. B.; Zhang, L.; Lee, K.; Liu, H.; Marques, A. L. B.; Marques, E. P.; Wang, H.; Zhang, J. A review of Fe-N/C and Co-N/C catalysts for the oxygen reduction reaction. *Electrochim. Acta* **2008**, *53*, 4937-4951; DOI 10.1016/j.electacta.2008.02.012.

(76) Ferrari, A. C.; Robertson, J. Interpretation of Raman spectra of disordered and amorphous carbon. *Phys. Rev. B* **2000**, *61*, 14095-14107; DOI 10.1103/PhysRevB.61.14095.

(77) Perazzolo, V.; Grądzka, E.; Durante, C.; Pilot, R.; Vicentini, N.; Rizzi, G. A.; Granozzi, G.; Gennaro, A. Chemical and electrochemical stability of nitrogen and sulphur doped mesoporous carbons. *Electrochim. Acta* **2016**, *197*, 251-262; DOI 10.1016/j.electacta.2016.02.025.

945 (78) Salmerón, I.; Plakas, K. V.; Sirés, I.; Oller, I.; Maldonado, M. I.; Karabelas, A. J.;
946 Malato, S. Optimization of electrocatalytic H_2O_2 production at pilot plant scale for solar-assisted
947 water treatment. *Appl. Catal. B: Environ.* **2019**, *242*, 327-336; DOI 10.1016/j.apcatb.2018.09.045.
948 (79) Steter, J. R.; Brillas, E.; Sirés, I. On the selection of the anode material for the
949 electrochemical removal of methylparaben from different aqueous media. *Electrochim. Acta* **2016**,
950 *222*, 1464-1474; DOI 10.1016/j.electacta.2016.11.125.
951 (80) Isarain-Chávez, E.; Arias, C.; Cabot, P. L.; Centellas, F.; Rodríguez, R. M.; Garrido,
952 J. A.; Brillas, E. Mineralization of the drug β-blocker atenolol by electro-Fenton and photoelectro-
953 Fenton using an air-diffusion cathode for H_2O_2 electrogeneration combined with a carbon-felt
954 cathode for Fe^{2+} regeneration. *Appl. Catal. B: Environ.* **2010**, *96*, 361-369; DOI
955 10.1016/j.apcatb.2010.02.033.
956 (81) Píšťková, V.; Tasbihi, M.; Vávrová, M.; Štangar, U. L. Photocatalytic degradation of
957 β-blockers by using immobilized titania/silica on glass slides. *J. Photochem. Photobiol. A: Chem.*
958 **2015**, *305*, 19-28; DOI 10.1016/j.jphotochem.2015.02.014.
959 (82) Xu, A.; Brillas, E.; Han, W.; Wang, L.; Sirés, I. On the positive effect of UVC light
960 during the removal of benzothiazoles by photoelectro-Fenton with UVA light. *Appl. Catal. B:*
961 *Environ.* **2019**, *259*, 118127; DOI 10.1016/j.apcatb.2019.118127.
962 (83) Nsubuga, H.; Basheer, C.; Jalilov, A.; Haider, M. B.; Al-Saadi, A. A. Droplet flow-
963 assisted heterogeneous electro-Fenton reactorfor degradation of beta-blockers: response surface
964 optimization, and mechanism elucidation. *Environ. Sci. Poll. Res.* **2019**, *26*, 14313-14327; DOI
965 10.1007/s11356-019-04551-1.
966

Figure captions

Figure 1. Different stages during the synthesis of MC-C catalysts: (a) chitosan viscous solution, (b) hydrogel coagulation (c) chitosan hydrogel, (d) hydrogel after freeze drying, (e) dried hydrogel after pyrolysis at 400 °C, (f) first pyrolysis product after milling, (g) product after pyrolysis at 900 °C.

Figure 2. TEM images of (a-c) MC-C and (d-f) N-MC-C catalysts.

Figure 3. (a) Nitrogen adsorption/desorption isotherms of MC-C and N-MC-C catalysts; (b) Raman spectra for both materials; C 1*s* XPS core-level spectra for (c) MC-C and (d) N-MC-C catalysts; N 1*s* XPS core-level spectra for (e) MC-C and (f) N-MC-C. In plot (c-f), deconvolution signals are also shown.

Figure 4. Electrochemical data for the investigated materials, drop-cast on glassy carbon (catalyst loading: 0.3 mg/cm^2), in Ar-purged and O_2-saturated 0.0005 M H_2SO_4 + 0.050 M Na_2SO_4 electrolyte. Cyclic voltammograms using (a) MC-C and (b) N-MC-C, at v_{scan} = 20 mV/s. Linear sweep voltammograms at RRDE, with at v_{scan} = 10 mV/s and ω = 1600 rpm, using (c) MC-C and (d) N-MC-C. (c', d') Ring current, at E_{ring} = 1.50 V vs. RHE, and (c", d") H_2O_2 selectivity during the linear sweep voltammetry in O_2-saturated electrolyte, using (c', c'`) MC-C and (d', d") N-MC-C.

Figure 5. Evolution of H_2O_2 concentration during the electrolysis of 150 mL of 0.050 M Na_2SO_4 solutions at pH 3.0 and 25 °C, using a cell with the MC-C or N-MC-C cathode and a DSA plate as the anode at different current densities and air flow rate of 36 L/h. Process: (a) EO-H_2O_2, and (b) EF with 0.50 mM Fe^{2+} and PEF with 0.50 mM Fe^{2+} and a 6 W UVA lamp.

Figure 6. Time course of acebutolol concentration during the treatment of 150 mL of solutions with 0.046 mM drug and 0.050 M Na_2SO_4 at pH 3.0 and 25 °C, using a cell with the MC-C or N-

MC-C cathode at a current density of 30 mA/cm^2 and air flow rate of 36 L/h. Process (a) EO-H_2O_2 with DSA, and (b) PEF with 0.50 mM Fe^{2+}, a 6 W UVA lamp and DSA or BDD as the anode. In (b), the inset panel presents the corresponding pseudo-first-order kinetic analysis.

Figure 7. Change of normalized TOC with electrolysis time for the PEF trials shown in Fig. 6b.

Figure 8. SEM images of GDEs prepared with the chitosan-based electrocatalysts. (a-d) Fresh and (a'-d') used. Magnification: (a,a',c,c') 100× and (b,b',d.d') 500×. The used GDEs were those collected at the end of the PEF treatments with DSA described in Fig.7.

Figure 9. Primary products of acebutolol during PEF treatment with chitosan-derived electrocatalysts.

Figure 10. Evolution of the concentration of aliphatic carboxylic acids during the PEF treatment of 0.046 mM acebutolol solutions with 0.050 M Na_2SO_4 and 0.50 mM Fe^{2+}, as well as NH_4^+ content accumulated during an analogous treatment but using 0.092 mM drug and 0.020 M Na_2SO_4 instead. Conditions: cell with N-MC-C cathode (fed with air at 36 L/h) and the RuO_2-based anode, containing 150 mL of solutions at pH 3.0 and 25 ºC exposed to a 6 W UVA lamp and electrolyzed at 30 mA/cm^2.

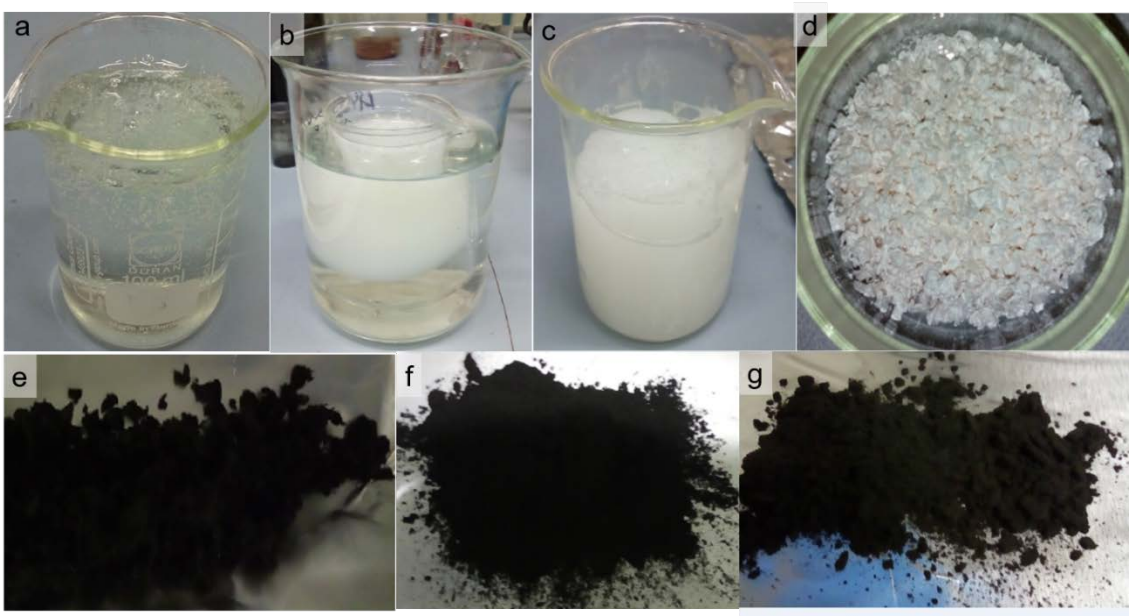

Figure 1

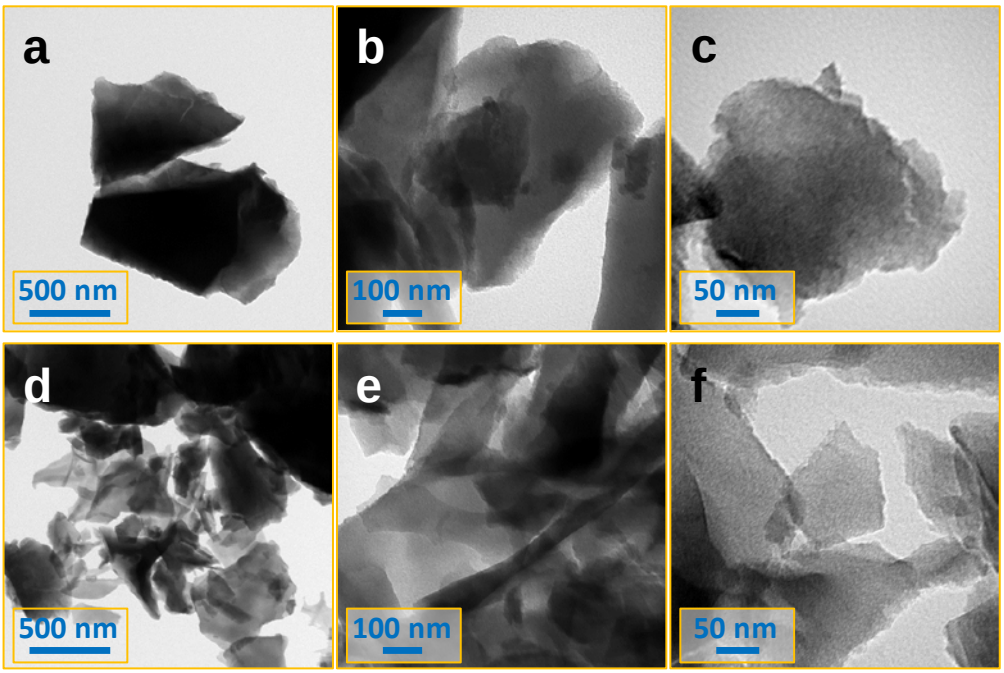

Figure 2

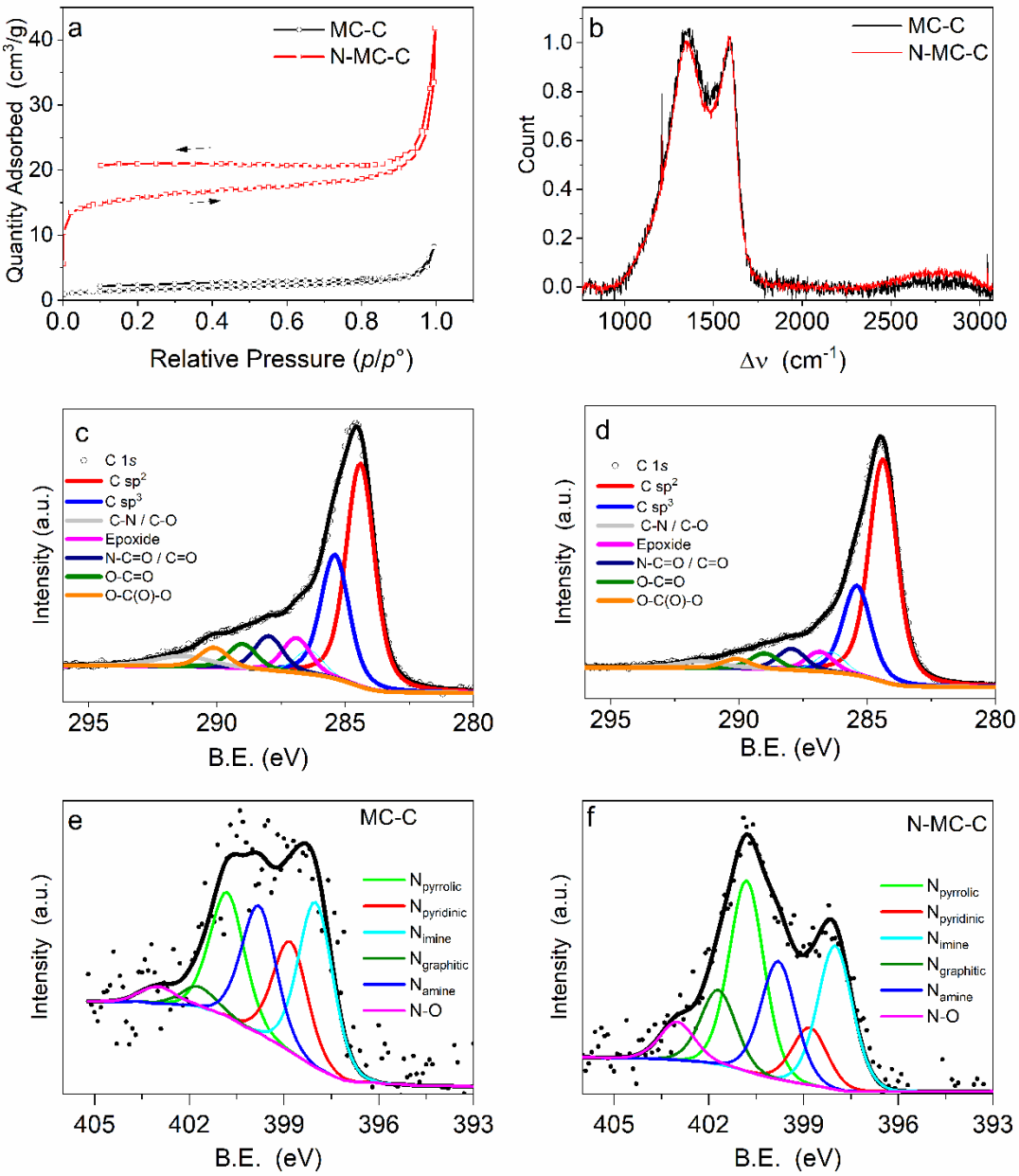
a
MC-C
N-MC-C
Quantity Adsorbed (cm3/g)
Relative Pressure (p/p°)
b
MC-C
N-MC-C
Count
Δν (cm-1)
c
C 1s
C sp2
C sp3
C-N / C-O
Epoxide
N-C=O / C=O
O-C=O
O-C(O)-O
Intensity (a.u.)
B.E. (eV)
d
C 1s
C sp2
C sp3
C-N / C-O
Epoxide
N-C=O / C=O
O-C=O
O-C(O)-O
Intensity (a.u.)
B.E. (eV)
e
MC-C
Npyrrolic
Npyridinic
Nimine
Ngraphitic
Namine
N-O
Intensity (a.u.)
B.E. (eV)
f
N-MC-C
Npyrrolic
Npyridinic
Nimine
Ngraphitic
Namine
N-O
Intensity (a.u.)
B.E. (eV)

Figure 3

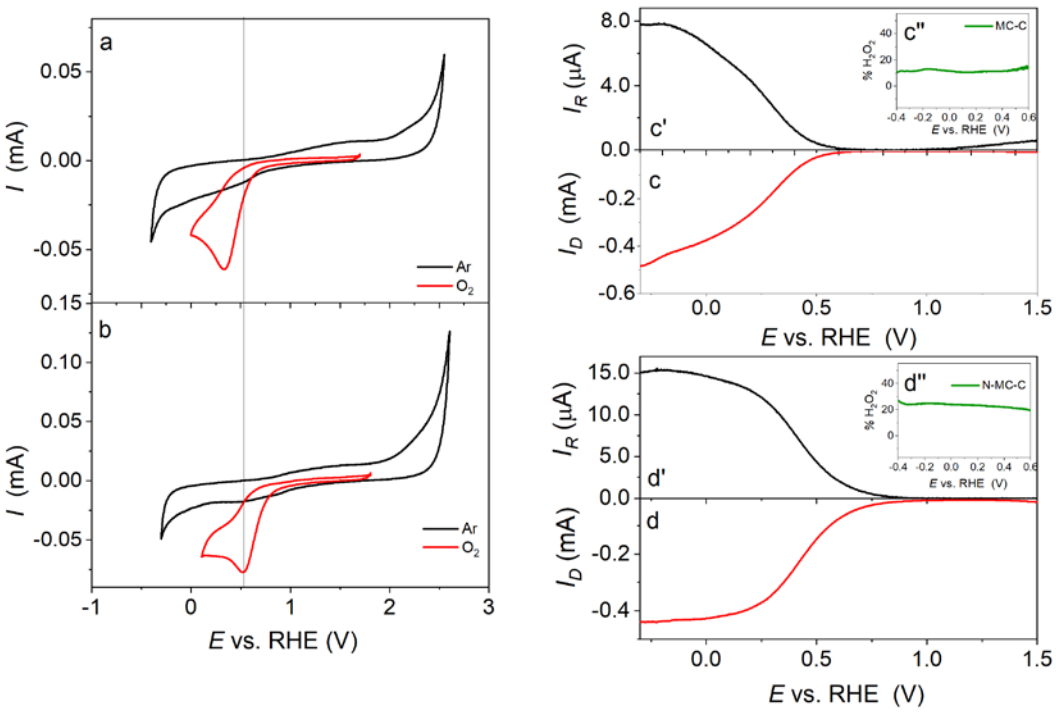

Figure 4

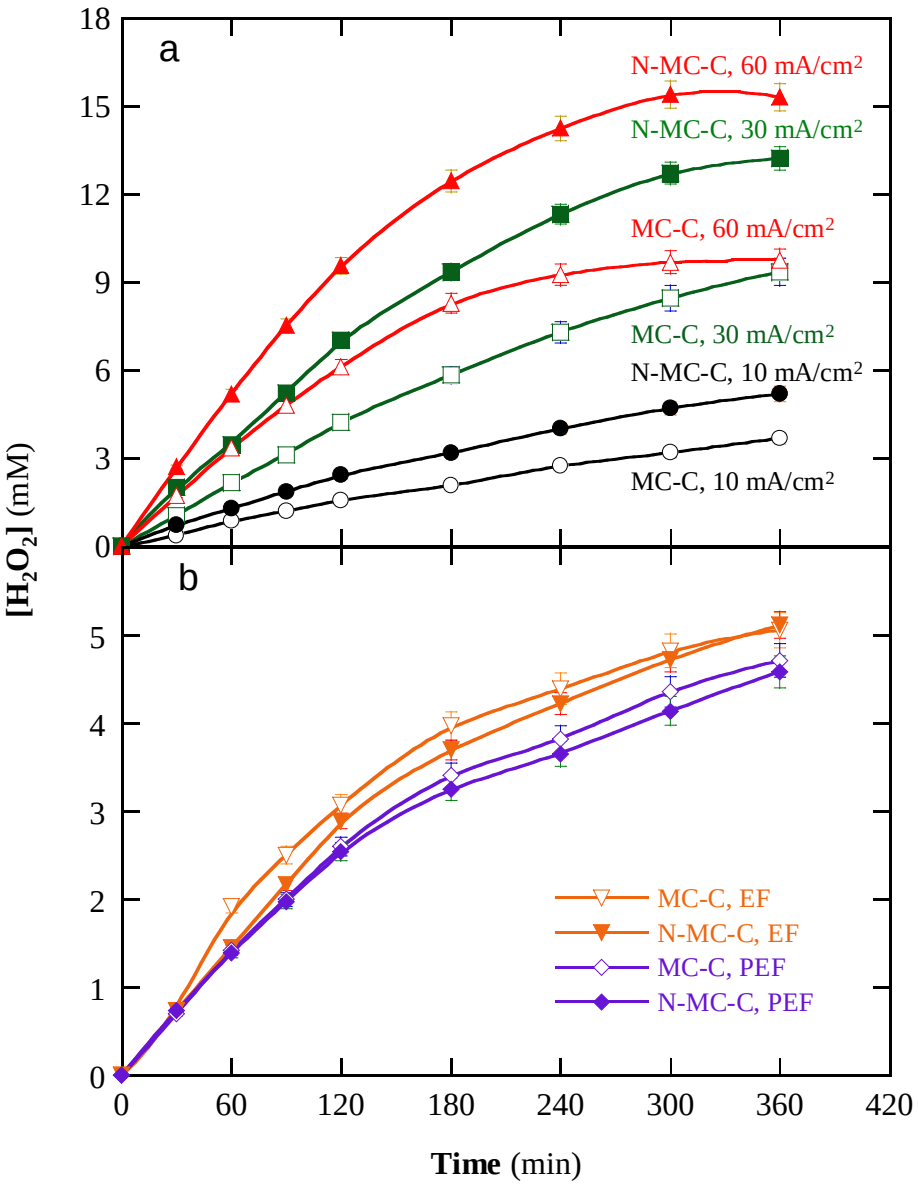
a
b
N-MC-C, 60 mA/cm²
N-MC-C, 30 mA/cm²
MC-C, 60 mA/cm²
MC-C, 30 mA/cm²
N-MC-C, 10 mA/cm²
MC-C, 10 mA/cm²
MC-C, EF
N-MC-C, EF
MC-C, PEF
N-MC-C, PEF
[H2O2] (mM)
Time (min)
0
3
6
9
12
15
18
1
2
4
5
60
120
180
240
300
360
420

Figure 5

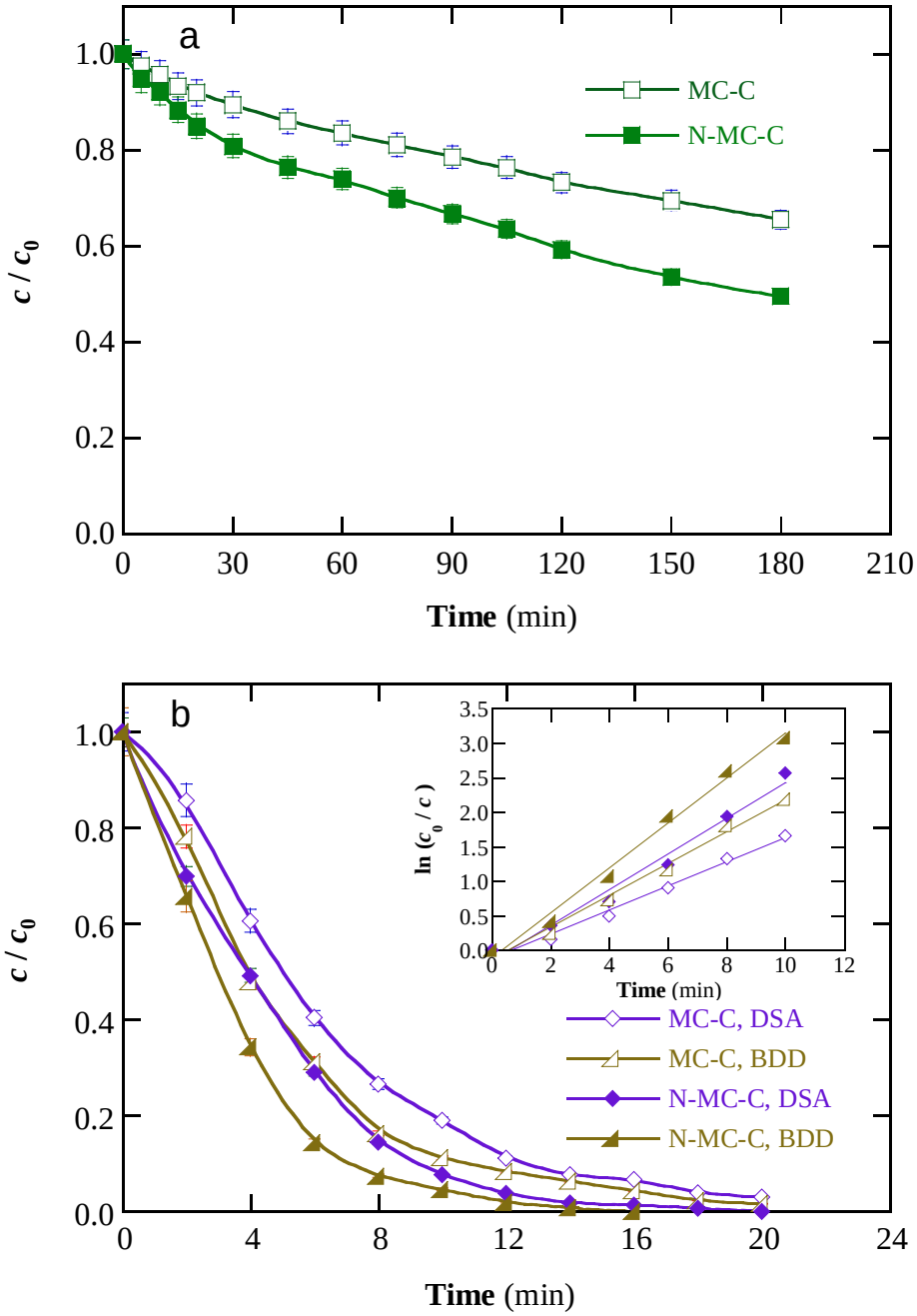
a
MC-C
N-MC-C
c / c0
Time (min)
b
MC-C, DSA
MC-C, BDD
N-MC-C, DSA
N-MC-C, BDD
ln (c0 / c)
Time (min)
c / c0
Time (min)

Figure 6

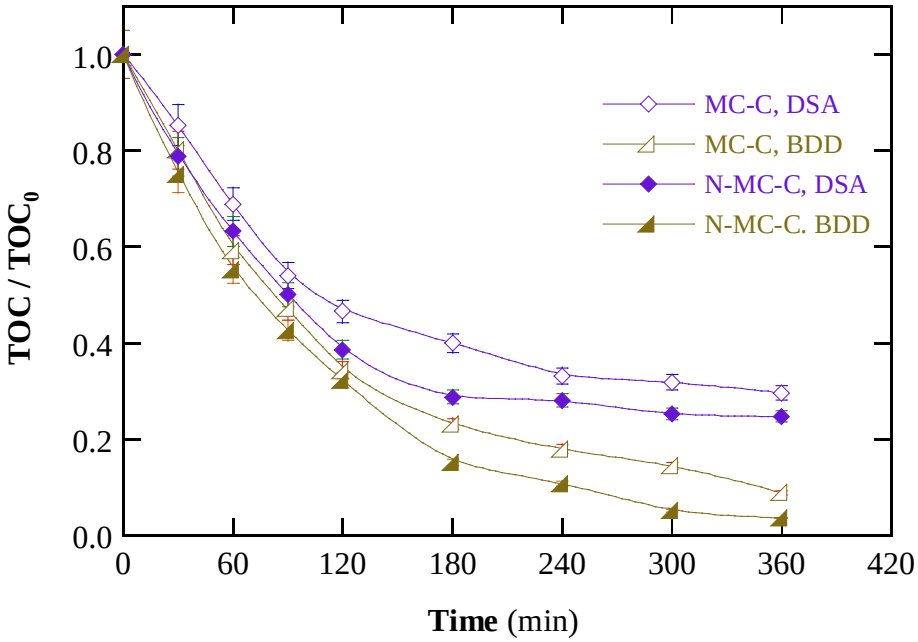
1.0
0.8
0.6
0.4
0.2
0.0
TOC / TOC0
0
60
120
180
240
300
360
420
Time (min)
MC-C, DSA
MC-C, BDD
N-MC-C, DSA
N-MC-C. BDD

Figure 7

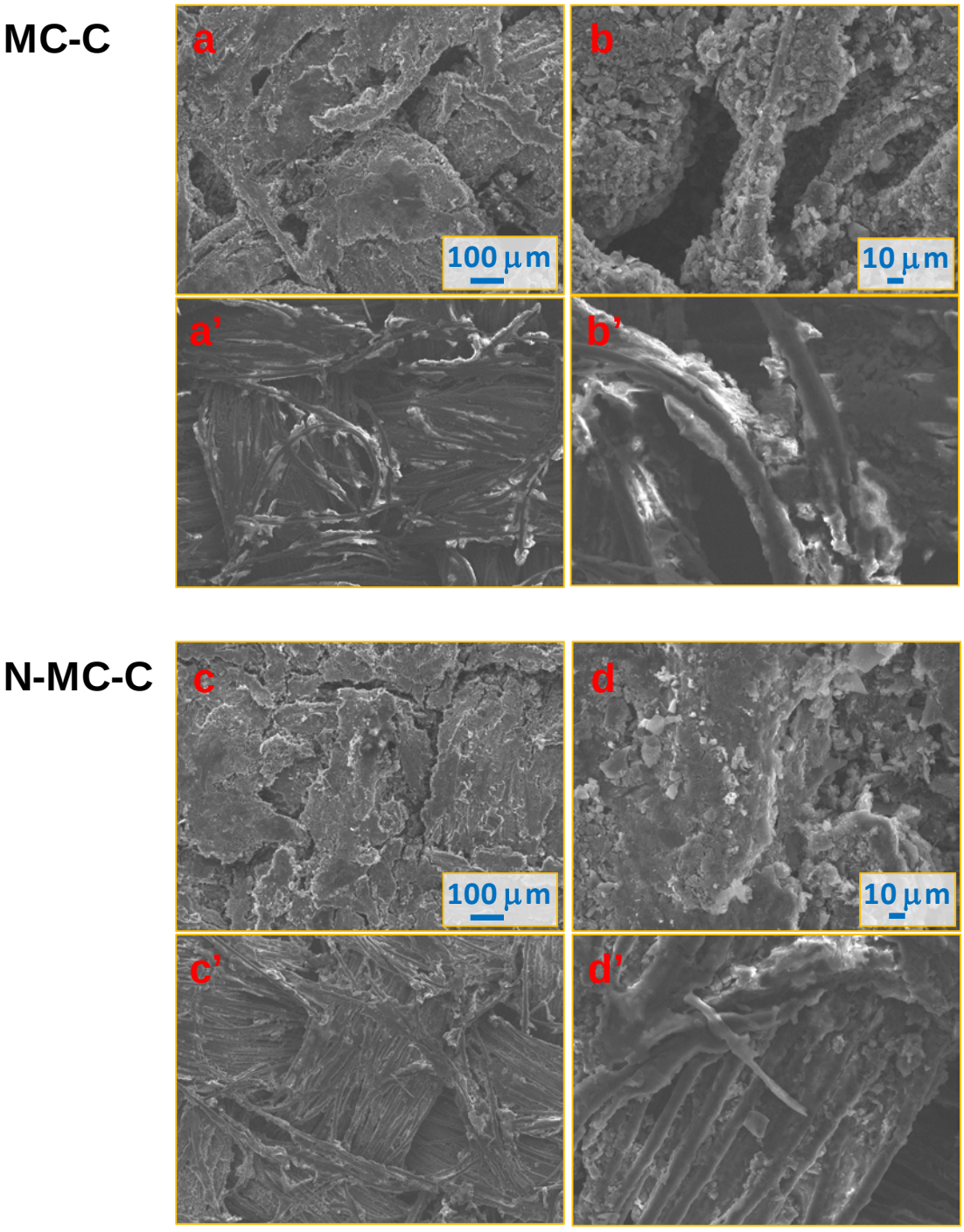

Figure 8

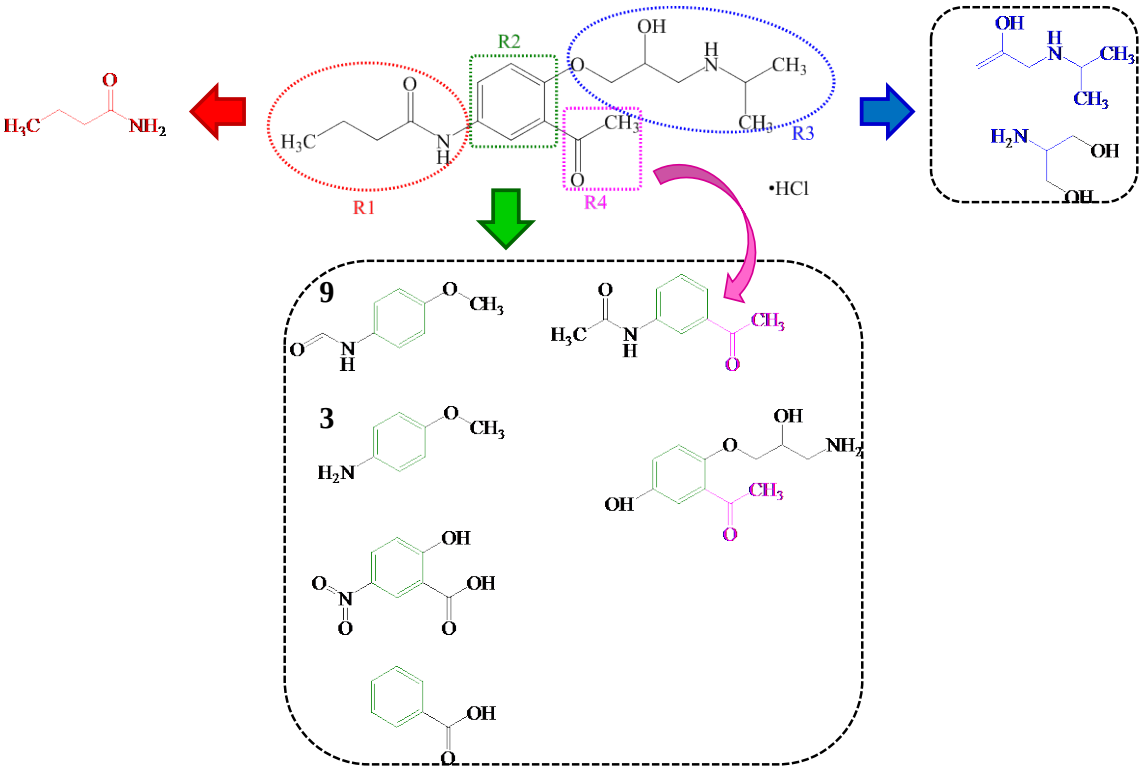

Figure 9

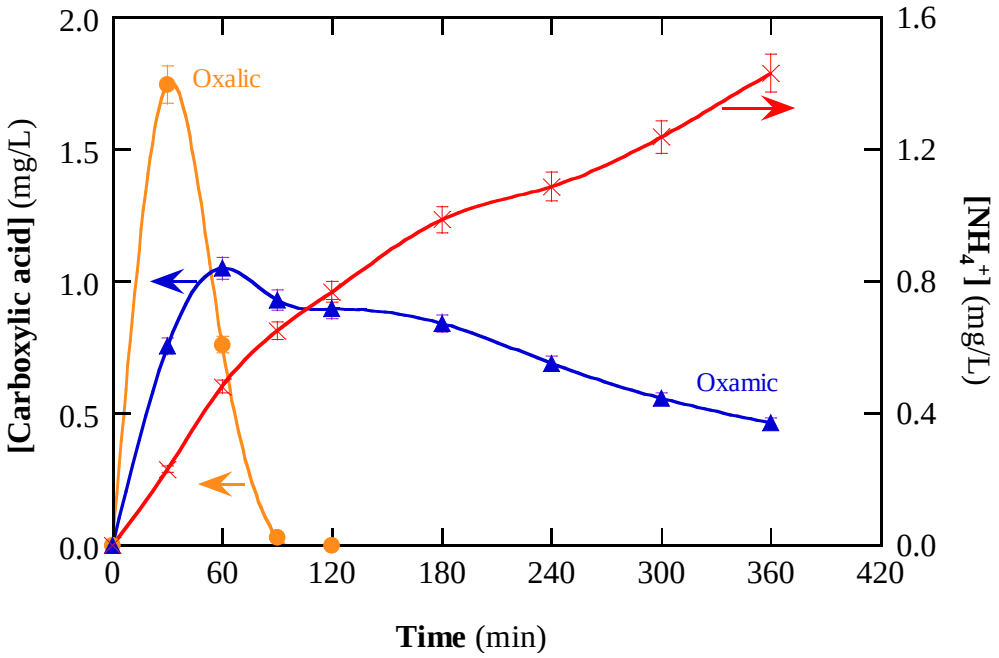
2.0
1.5
1.0
0.5
0.0
1.6
1.2
0.8
0.4
0.0
0
60
120
180
240
300
360
420
Oxalic
Oxamic
[Carboxylic acid] (mg/L)
[NH4+] (mg/L)
Time (min)

Figure 10

Table 1

Chemical and textural properties of activated carbons.

Sample	C[a] (%)	H[a] (%)	N[a] (%)	A_{BET}[b] (m^2/g)	V_{TOT}[b] (cm^3/g)	V_{μ}[b] (cm^3/g)	V_{meso}[b] (cm^3/g)	V_{DFT}[b] (cm^3/g)
MC-C	76.44	0.81	6.81	6	0.013	0.002	0.005	0.007
N-MC-C	79.39	1.73	4.62	63	0.065	0.021	0.017	0.038

Sample	C 1s[c] (at %)	O 1s[c] (at %)	N 1s[c] (at %)	N_{imine}[c] (%)	$N_{pyridinic}$[c] (%)	N_{aminic}[c] (%)	$N_{pyrrolic}$[c] (%)	$N_{graphitic}$[c] (%)	N-O[c] (%)
MC-C	78.5	19.1	2.4	29.3	19.5	22.7	22.0	3.5	3.0
N-MC-C	81.6	15.3	3.1	23.1	9.2	19.0	30.7	12	6.1

[a] Elemental analysis determined by CHN analyser.

[b] Texture properties determined from nitrogen adsorption-desorption isotherms.

[c] Elemental analysis expressed in atomic percentage and nitrogen functionalities determined from XPS analysis and N 1*s* spectra deconvolution.

TABLE OF CONTENTS (TOC) ART

For Table of Contents Use Only.

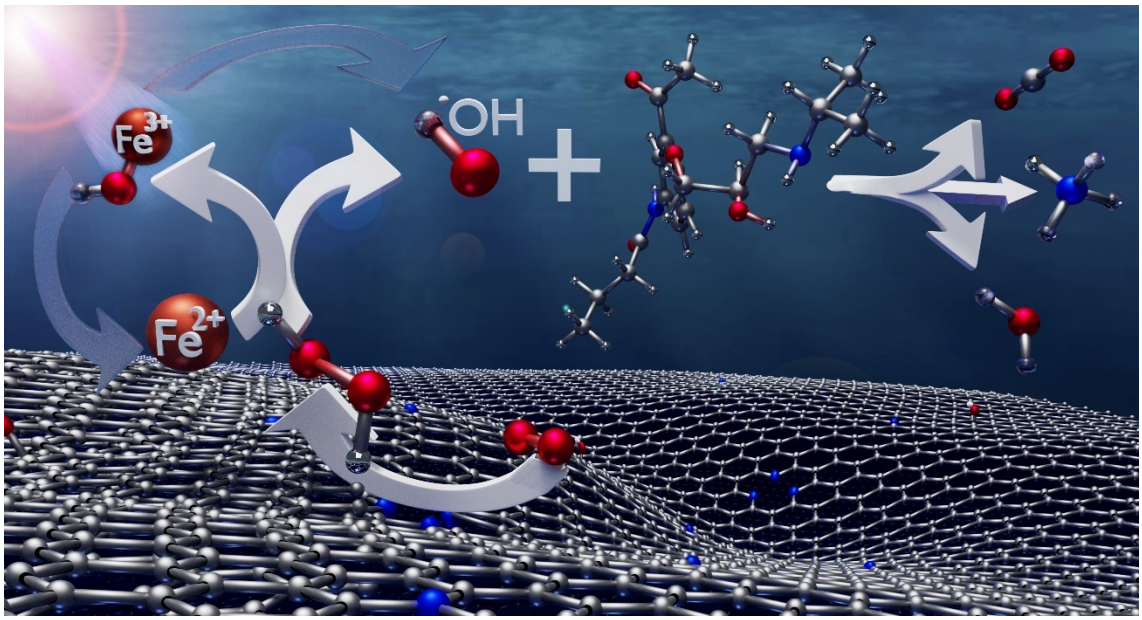

A more sustainable H_2O_2 electrosynthesis from O_2 reduction, aiming at $^{\bullet}OH$-mediated water treatment, by employing an air-diffusion cathode with biomass-derived N-doped carbon